Eruptive dynamics of the 2021 Tajogaite eruption (La Palma, Canary Islands) as revealed by the physical and textural characterization of tephra

Serena Da Mommio[1], Marija Voloschina[1], Beverley C. Coldwell[2,3], Nemesio M. Pérez[2,3], Costanza Bonadonna[4], Marco Pistolesi[1]

1. Department of Earth Sciences, University of Pisa, Pisa, Italy
2. Instituto Volcanológico de Canarias (INVOLCAN), Puerto de la Cruz, Santa Cruz de Tenerife, Canary Islands, Spain
3. Environmental Research Division, Instituto Tecnológico y de Energías Renovables (ITER), Granadilla de Abona, Santa Cruz de Tenerife, Canary Islands, Spain
4. Department of Earth Sciences, University of Geneva, Geneva, Switzerland

Serena Da Mommio https://orcid.org/0009-0001-7487-2237
Marija Voloschina https://orcid.org/0000-0002-7568-6495
Beverley C. Coldwell https://orcid.org/0000-0001-9240-6240
Nemesio M. Pérez https://orcid.org/0000-0003-1410-7717
Costanza Bonadonna https://orcid.org/0000-0002-2368-2193
Marco Pistolesi https://orcid.org/0000-0002-5096-3708

Corresponding author: Serena Da Mommio serena.damommio@phd.unipi.it

Abstract

A multidisciplinary study of juvenile material ejected during the September-December 2021 eruption of Tajogaite volcano (La Palma, Canary Islands) was conducted to understand the processes that occurred during pre-eruptive magma ascent and within the conduit system, in order to obtain a reconstruction of the eruptive dynamics. Variations in the physical, morphological, textural, and chemical characteristics of the juvenile material reveal changes in the mechanisms of outgassing, fragmentation, and velocity of magma ascent within the conduits. In agreement with the three main identified eruptive phases, we found that: Phase I corresponds to the maximum eruption intensity, when highly vesicular clasts were produced, which show primary vesicularity modes between 54.7 and 68.0% decreasing from the base to the top of this phase and N_v^m values between 11.4 and 16.6×10^6 cm^{-3}. Morphological parameters show high solidity, medium to low convexity values and low axial ratios, indicating the presence of clasts with predominantly irregular morphology and rough and spongy outer surfaces. Phase II was initially characterized by a lower eruptive intensity, producing dense juvenile material with irregular to subspherical morphologies, and afterwards by explosive activity characterized by intermittent episodes of variable intensity. Phase II clasts show vesicularity modes between 60.3 and 61.2 % and N_v^m values between 14.6 and $42.0\cdot\times 10^6$ cm^{-3}. Solidity values are high while convexity values cover a wider range indicating the presence of clasts with both smooth and rough external surfaces. Phase III was characterized by a new increase in eruptive intensity with clasts that show a vesicularity mode at ~60.2 % and average N_v^m values ranging from 24.0 to 85.2×10^6 cm^{-3}. The morphology of the clasts is variable, while solidity and convexity values are higher than the other phases. Syn-eruptive variability confirmed the presence of multiple conduits simultaneously active and defined by different geometries that regulated the processes of outgassing, fragmentation and crystallization of magma as it ascended to the surface. The tephra clasts are compositionally grouped in the

tephrite-basanite field, with a decreasing degree of magma evolution as the eruption progressed but during which observed variations could be associated with repeated (more primitive) magmatic inputs that fuelled the eruption over time.

Keywords

Tephra deposit - Hybrid eruption – Vesicularity - Eruptive style

Introduction

Hybrid eruptions refer to a specific type of volcanic eruption that exhibits mixed effusive and explosive behavior occurring simultaneously or in a very short succession (Pioli et al. 2009, Bonadonna et al. 2022). This activity has been observed and well characterized at some case studies, such as Parìcutin volcano (Pioli et al. 2009), Etna volcano (Taddeucci et al. 2002; 2004) and Tajogaite volcano (Bonadonna et al. 2022, 2023). In these examples, field observations combined with detailed analyses and numerical models showed how different parameters of the magmatic system can change during the eruption. These parameters include different depths of magma storage and accumulation times, the ascent rate, variations in magma/gas ratios, particular conduit geometries and variations in magma composition. Changes in the magmatic system are reflected in the production of a wide range of juvenile material that differs in physical, morphological, textural, and compositional characteristics (Taddeucci et al. 2023). For example, grain-size changes in clasts can reflect fluctuations in eruption intensity and fragmentation mechanisms (Bonadonna et al. 2023), variations in morphological parameters can provide information on the efficiency of magmatic fragmentation (Cioni et al. 2014), and variations in textural characteristics can be related to gas supply, magma residence time and ascent rate (Cioni et al. 2014, Taddeucci et al. 2023, Zanon et al. 2024). To better understand the mechanisms that occur during syn-eruptive and pre-eruptive magma ascent in these particular eruptions, we present a detailed study of the juvenile material, taking into account the variability that occurs from the beginning to the end of the eruption.

The Tajogaite eruption of Cumbre Vieja volcano of La Palma (Canary Islands, Spain) began on 19 September 2021 with the opening of a fissure on the western flank of the Cumbre Vieja rift zone and lasted 86 days (Bonadonna et al. 2022; Carracedo et al. 2022; Romero et al. 2022; Rodríguez et al. 2024). The eruption immediately featured explosive-effusive eruptive activity, with alternating, or more often simultaneous, emission of lava flows and tephra from different eruptive vents. The vents located at the base of the Tajogaite cone, which formed within a short time from the beginning of the eruption (Civico et al. 2022; Romero et al. 2022), generated mainly effusive activity, while the summit vents were associated with explosive activity with pulsating plumes that deposited a widespread tephra blanket. The eruption was classified as a long-lasting hybrid eruption, associated with a decoupled magma-gas system (Bonadonna et al. 2022). Although pyroclastic material constituted only 7-16% of the total volume erupted, the study of the associated tephra deposits provides fundamental insights into the dynamics of this eruption. Over the past three years, extensive research efforts have been dedicated to the study of the September-December 2021 Tajogaite eruption. Recent papers focused on specific aspects of the eruption (sedimentology, petrography, seismicity, surface deformation, and variations in eruptive activity; Bonadonna et al. 2022,2023; Carracedo et al. 2022; Civico et al. 2022; D'Auria et al. 2022; De Luca et al, 2022; Pankhurst et al, 2022; Rodríguez et al. 2024; Romero et al., 2022; Taddeucci et al. 2023; Ubide et al. 2023; Zanon et al. 2024). In the physical volcanology studies by Bonadonna et al. (2022, 2023), a detailed characterisation of the tephra blanket was carried out, which allowed a reconstruction of the dynamics of dispersion and deposition during the eruption. Combining this data with information on atmospheric wind, volcanic tremor and lava emission rates, the studies revealed significant changes in eruptive style and intensity. Based on microthermometry of fluid inclusions, Zanon et al. (2024) suggest that the eruption was fuelled by groups of magmas with distinct petrographic and geochemical features that accumulated at different depths and then ascended at different rates. Finally, in the geochemical study by Ubide et al. (2023), variations in the chemical composition of the magma were found for the elements Zr, Nd and SiO_2 and for the $^{87}Sr/^{86}Sr$ ratios, demonstrating the presence of mixing phenomena and different deep magmatic inputs that fuelled the eruption. However, what is lacking so far is a detailed study of the fine-grained tephra particles that addresses the changes in physical, morphological, textural, and compositional characteristics with eruption progression, and which may elucidate the processes occurring within the conduit with the goal of reconstructing the variable eruptive dynamics.

In this paper we propose a multidisciplinary study for the characterization of tephra deposits that aims to reconstruct the dynamics of magma ascent and fragmentation in eruptions characterized by contemporary different styles. We present morphological, textural, and geochemical analyses of representative tephra layers, investigating the variability of the products within each eruptive phase and the progressive change of these characteristics. The aim is to contribute to the understanding of the processes that occurred within the feeding system of the Tajogaite 2021 eruption as well as discussing the possible mechanisms and parameters controlling the observed shift in eruptive activity over time.

1. Geological context and chronology of the 2021 Tajogaite eruption

La Palma is the most active volcanic island of the Canary archipelago, and its formation began 3-4 Ma ago as a basal submarine seamount complex (Staudigel et al. 1986; Carracedo et al. 1998; 1999). Subaerial activity, which began around 1.8 Ma ago, built the Garafía and Taburiente shield volcanoes and the Cumbre Nueva rift in the northern sector of the island (Guillou et al. 1998; 2001). Subsequently, eruptive activity moved southwards, forming the Cumbre Vieja rift zone, which represents the currently active magmatic system of La Palma. The island's historical eruptions have often occurred simultaneously from multiple eruptive vents, and eight eruptions have occurred since the 15^{th} century (1480, 1585, 1646, 1677, 1712, 1949, 1971 and 2021), characterized mainly by both explosive and effusive character (Klügel al. 2000; 2017; Carracedo et al. 2001; Pankhurst et al. 2022).

The 2021 Tajogaite eruption occurred after 50 years of quiescence and was the largest eruptive event in the history of La Palma. It was preceded by relatively deep (10-25 km) and low-magnitude (Mw <2) seismic swarms since 2017, increased ground deformation, and detection of geochemical anomalies (D'Auria, et al. 2022, Di Nardo et al. 2022; Rodríguez-Pérez et al. 2022). In the week prior to the eruption, a migration of seismicity toward the surface was observed, interpreted as magma rising to the surface (D'Auria et al. 2022).

The eruption officially started on 19 September 2021 with the opening of a new eruptive vent in the Cabeza de Vaca area (locality of El Paso), situated on the western flank of the Cumbre Vieja rift, and ended on 14 December. During this period, the eruption was characterized by simultaneous effusive and explosive activity. The explosive activity was marked by Strombolian explosions alternating with lava fountaining, while effusive activity produced lava flows that descended toward the ocean in the western part of the island (Bonadonna et al. 2022; Carracedo et al. 2022; Romero et al. 2022; Taddeucci et al. 2023). Within a short time from the start of activity, a monogenic volcanic edifice was formed (Volcán de Tajogaite; Fig. 1), consisting of the accumulation of lava, ash, lapilli and spatter and defined successively by six eruptive vents aligned NW-SE for about 560 m. The summit vents located in the NE sector of the cone were associated with explosive activity, while the vents located at lower elevations to the SW part of the cone generated predominantly effusive activity. Effusive activity generated a lava field of ~12 km² on the western flank of the island, reaching the sea, while explosive activity produced pulsating plumes of varying heights (observed up to 8.5 km above sea level) and a widespread tephra blanket (Carracedo et al. 2022; Civico et al. 2022; Bonadonna et. al. 2022, 2023; Rodríguez et al. 2024).

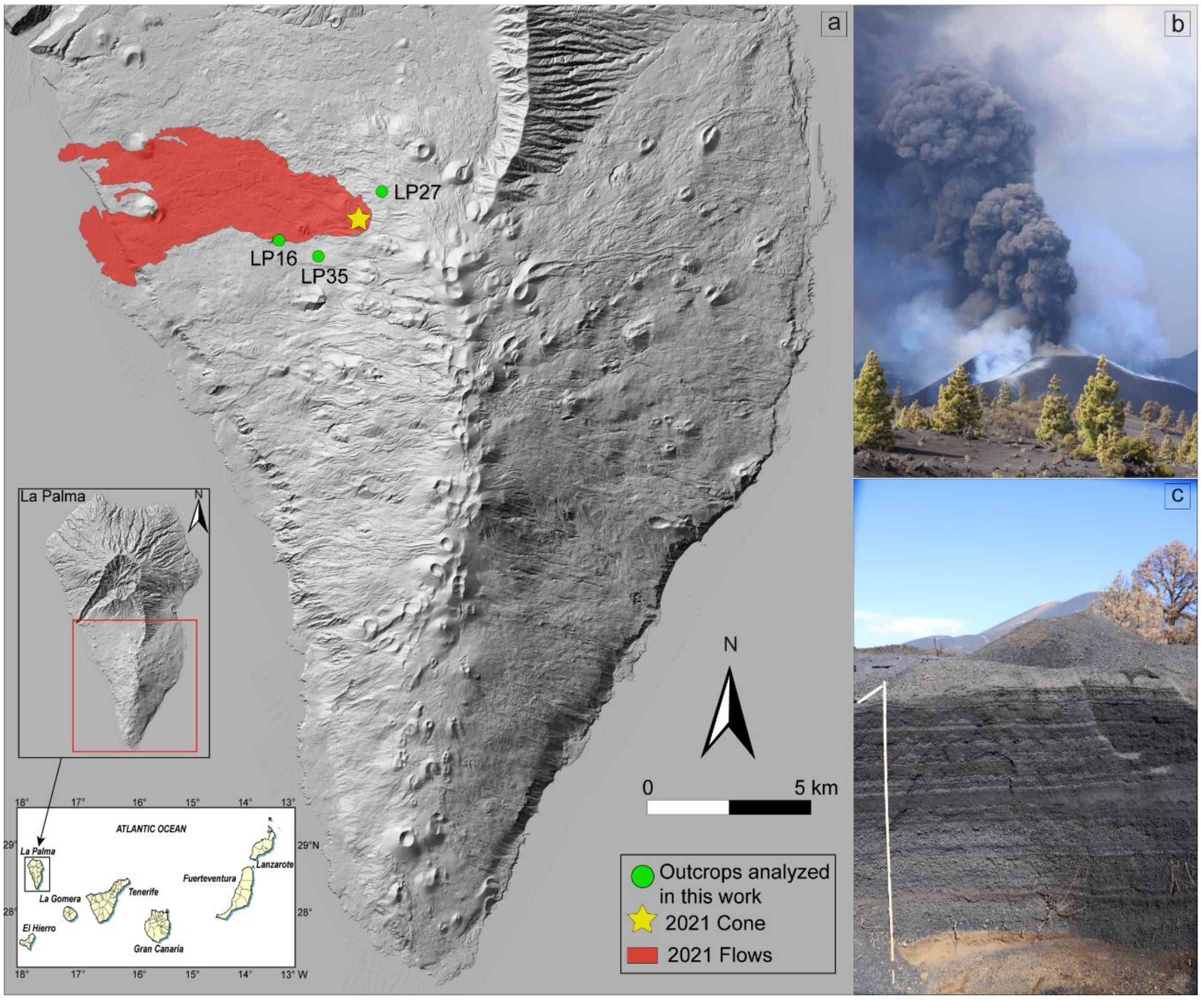

Fig. 1 a) Geographical location of La Palma and the Cumbre Vieja rift zone, located in the southern half of the island. Digital Elevation Model of La Palma from the Centro Nacional de Informació Geográfica (Ministerio de Transportes, Movilidad y Agenda Urbana of Spain) b) Explosive activity with formation of ash-rich eruptive

columns from the main vent. c) Outcrops LP35 (182 cm-thick), located ∼1 km SW of the cone (Bonadonna et al., 2023)

Among the tephra particles emitted during the eruption, bombs mostly followed ballistic trajectories falling in areas close to the eruptive vents (generally less than a km away), while ash and lapilli were dispersed hundreds of kilometers from the cone (Carracedo et al., 2022). The tephra blanket was distributed mainly in a NE-SW direction due to complex regional and local wind patterns, and deposits reached thicknesses of more than a meter at distances of 1 km from the eruptive vents (Bonadonna et al. 2022; Fig. 1c).

The tephra sequence was subdivided into units, layers, and sublayers that represent changes in eruptive style and dynamics throughout the entire activity (Romero et al. 2022; Bonadonna et al. 2022, 2023). Specifically, eleven layers and eighteen sublayers were identified within the eruptive sequence, grouped into three different tephra units: The Lower Unit (LU) is a lapilli-size dominated unit intercalated with fine-to-coarse ash; it is made of three layers (LU1, LU2, and LU3), which can be further subdivided in sublayers (LU1.1 to LU2.4) and comprises the coarsest deposits of the eruption. The Middle Unit (MU) is a fine-to-coarse-ash-dominated unit intercalated with lapilli layers; it is made of six layers (MU1, MU2, MU3, MU4, MU5, MU6), with MU3 and MU6 being further subdivided in eight sublayers (MU3.1-3 and MU6.1-6). The Upper Unit (UU) closes the whole tephra sequence and represents the final part of the eruption. It is dominated by lapilli-sized clasts with a final phase characterized by bomb emission and consists of two main layers (UU1 and UU2).

Average plume heights are estimated at ~3.2 km a.s.l. and the total erupted volume (pyroclastic deposits and lava) is >200 million m^3 (Carracedo et al. 2022; Bonadonna et al. 2022, 2023). In addition, the emission of volcanic gases, particularly CO_2 and SO_2, had long-term consequences on the environment by affecting air quality in the surrounding areas and endangering the health of residents (Reyes-Hardy et al. 2024), while tephra deposits may continue to pose respiratory health hazards (Wertheim et al., 2023). Thanks to the monitoring and emergency management activities, there were no casualties. However, the Tajogaite eruption significantly affected the western part of the island, causing the evacuation of nearly 8000 people and damaging numerous buildings (Reyes-Hardy et al. 2024).

2. Methods

2.1 Sampling strategy

Two field campaigns were conducted both during (October-November 2021) and after the eruption (February and May 2022) to characterize the eruption deposit stratigraphy in collaboration with the Instituto Volcanológico de Canarias (INVOLCAN). The products selected for the studies in this paper were collected in two stratigraphic sections named LP27 and LP35 and located ~1 km NE and ~1 km SW of the eruptive vent, respectively. Sample MU1 was taken at LP16 located ~2 km SW of the vent.

Referring to the units described above (Lower Unit, Middle Unit and Upper Unit), thirteen tephra samples from LP35, collected along the eruptive sequence, were analyzed in this work and characterized from a sedimentological, textural, morphological and geochemical point of view; six samples represent the Lower Unit (LU1.1, LU1.6, LU2.1, LU2.3, LU3base, LU3top), five the Middle Unit (MU1, MU3.3, MU5, MU6.2 and MU6.4) and two the Upper Unit (UU1, UU2). In addition, six additional samples for density analysis were collected along the stratigraphic sequence at LP27 (LU1, LU2, LU3, MU3, MU5 and UU).

2.2 Grain-size data and componentry analyses

Samples for grain-size analysis were mechanically dry-sieved at half-ϕ intervals ($\phi = -\log_2 D$, where D is the particle diameter in millimeters) for the coarser fraction >1 mm. The fraction <1 mm was analysed with a particle size analyzer (RETSCH CamSizer); grain-size parameters were calculated according to Inman (1952) and Folk and Ward (1957). The coarse fraction clasts (grain-size >1 mm) from the different selected layers of the tephra sequence were analyzed for componentry; components from each grain-size class were separated by hand picking under a binocular microscope and weighed.

2.3 Physical and textural characterization of tephra particles

Density

Density measurements were performed on lapilli clasts (range 2-4 cm) collected along the stratigraphic sequence at LP35 (~1 km SW of the vent) for layers LU1.1, LU1.2, LU1.6, LU2.3, LU3, MU3, MU5, UU and at LP27 (~1 km NE of the vent), for layers LU1, LU2, LU3, MU3, MU5 and UU. Measurements were performed on 100 clasts per each layer and followed the method of Houghton and Wilson (1989) by determining weights in air and water after sealing. Clast densities were converted to 3D vesicularity values by using a dense rock equivalent (DRE) of 2,700 kg/m^3 and following Houghton and Wilson (1989). Density values are reported as distributions.

Morphological and textural analysis

For the main juvenile componentry groups, representative clasts were chosen by hand-picking under an optical microscope. A total of 186 juvenile fragments were mounted on slides using double-adhesive conductive carbon tape. The clasts were photographed with a stereomicroscope and a scanning electron microscope (SEM), and their external, 3D morphology was described in secondary electron mode (SE). The glass-slides containing the selected clasts were then embedded in epoxy resin, and polished to expose an area containing approximately the maximum diameter of the fragments. These slides were used for SEM imaging, particularly for the acquisition of backscattered electron images (BSE) used for 2D textural characterization of the same clasts previously described by their 3D morphology.

Morphological parameters were obtained through image analysis from scanning electron images. The projection of the particle outline on the horizontal plane was used as a proxy for the particle shape and the outline was filled and converted into a binary image, using ImageJ software (Schneider et al. 2012). Particle shape irregularities were measured with reference to an ellipse of equivalent area (major axis and minor axis), a bounding rectangle (BX width and BY height), and a convex bounding basin (CH area and CH perimeter; Liu et al. 2015). Other morphological parameters calculated were solidity (projected clast area/convex hull area), convexity (perimeter of the best-fit ellipse/perimeter of the clast), concavity index ($\sqrt{(1-S)^2+(1+C)^2}$, where S is the solidity and C is the convexity; Liu et al. 2015), and ellipse aspect ratio (minimum axis/maximum axis of the ellipse enclosing the particle). Solidity and convexity are inversely related to the complexity of the particle's outer surface; smooth and straight surfaces correspond to high values of solidity and convexity close to 1, while vesiculated particles with rough outer surfaces are represented by the lowest values. The ellipse aspect ratio reflects particle elongation with values close to 1 generally indicating spherical particles, while the convexity index (CI) is used to distinguish dense from vesiculated fragments; generally, low CI values are indicative of dense fragments.

Textural parameters such as vesicle number (N_V), shape and size distribution (VSD) were obtained from SEM-BSE images and then analyzed with ImageJ software. The different phases (vesicles and phenocrysts) recognized on the images were separated and saved on different binary images, and their shape, size and area were measured. The vesicles that showed signs of coalescence and broken septa were manually reconstructed to obtain their original size parameters. For each analyzed clast, a series of parameters was entered on an Excel spreadsheet in order to calculate the clast reference area, phenocryst content, and 2D vesicularity. The latter was estimated by relating the total area occupied by the bubbles to the clast reference area. Finally, the 2D data obtained from image analysis were converted to 3D using the stereological model of Sahagian and Proussevitch (1998), which allows to derive N_V (number of vesicles per unit volume), under the assumption of spherical vesicles. Vesicle numbers N_V were then corrected relative to melt volume (N_V^m), accounting for clast vesicularity. Because vesicles vary significantly in both size and number, data are displayed as distributions (Shea et al., 2010). Vesicle Volume Distribution (VVD) were used to derive information about the processes of bubble nucleation and/or coalescence, while Vesicle Size Distribution (VSD) provide insights into the kinematics of nucleation density and bubble growth rate (e.g., Marsh, 1988, 1998).

Compositional analyses

Composition of the glass matrix was obtained for 108 different juvenile fragments. For each clast, two to three measurements were made on selected points of the glass matrix, yielding a total of 250 analyses.

Major element analyses were performed using an electron microprobe analyzer (EMPA), model JEOL-JXA 8230, equipped with 5 WDS spectrometers and a solid-state EDS-SDD detector, at the MEMA center (University of Florence). Measurements were acquired with accelerating voltages of 15 kV, beam current of 5nA and beam spot sizes of 5 to 10 µm. To ensure consistency of results, glass standard Lipari ID3506, CFA-47, ATHO-G, Gor 128G, and STHS 6/80 were also analysed. Analytical errors for the elements analysed are: SiO_2 ± 0.39%, TiO_2 ± 1.18%, Al_2O_3 ± 0.63%, FeO ± 2.02% , MnO ± 15.57%, MgO ± 1.46%, CaO ± 0.61%, Na_2O ± 2.03%, K_2O ± 1.19%, P_2O5 ± 3.59%. Finally, average values and standard deviations were calculated for each analyzed clast.

3. Results

3.1 Grain-size and componentry

The samples analyzed in this work cover the three main units of the entire eruptive sequence, from base to top, and are considered to be representative of the entire eruption.

Grain-size analysis was performed on selected layers of tephra belonging to deposit LP35, located ∼1 km SW of the vent. Layer MU1 was sampled at LP16 (Bonadonna et al. 2022), located ~2 km SW of the vent. Grain-size data of the specific layers indicates a variability along the eruptive sequence. In the first eruptive phase (layer LU1.1), clasts show the coarsest grain-size with Mdϕ = -1.98, which then decreases as the eruption progresses (LU1 to LU3; Mdϕ -1.98 to -0.24). In the Middle Unit, the first layer MU1 shows the finest grain-size with Mdϕ=1.22, while MU3.3 and MU5, show Mdϕ values of -1.11 and -1.33, respectively, highlighting an increase in grain-size for these specific sublayers. The final layer of MU (MU6) is characterized by finer grain-size clasts (MU6.2 and MU6.4; Mdϕ between -0.86 and -0.29). In the last eruptive phase (samples/layers UU1 and UU2), the particle size increases again until the end of the eruption (Mdϕ between -0.62 and -1.11; Fig. 2b). In general, the samples show a unimodal particle size distribution with a secondary tail toward the finer grain-size fractions (Fig. 2a). The analysed tephra layers show good sorting with σϕ values ranging from 0.89 (for MU1) to 1.44 (for UU2; Fig. 2).

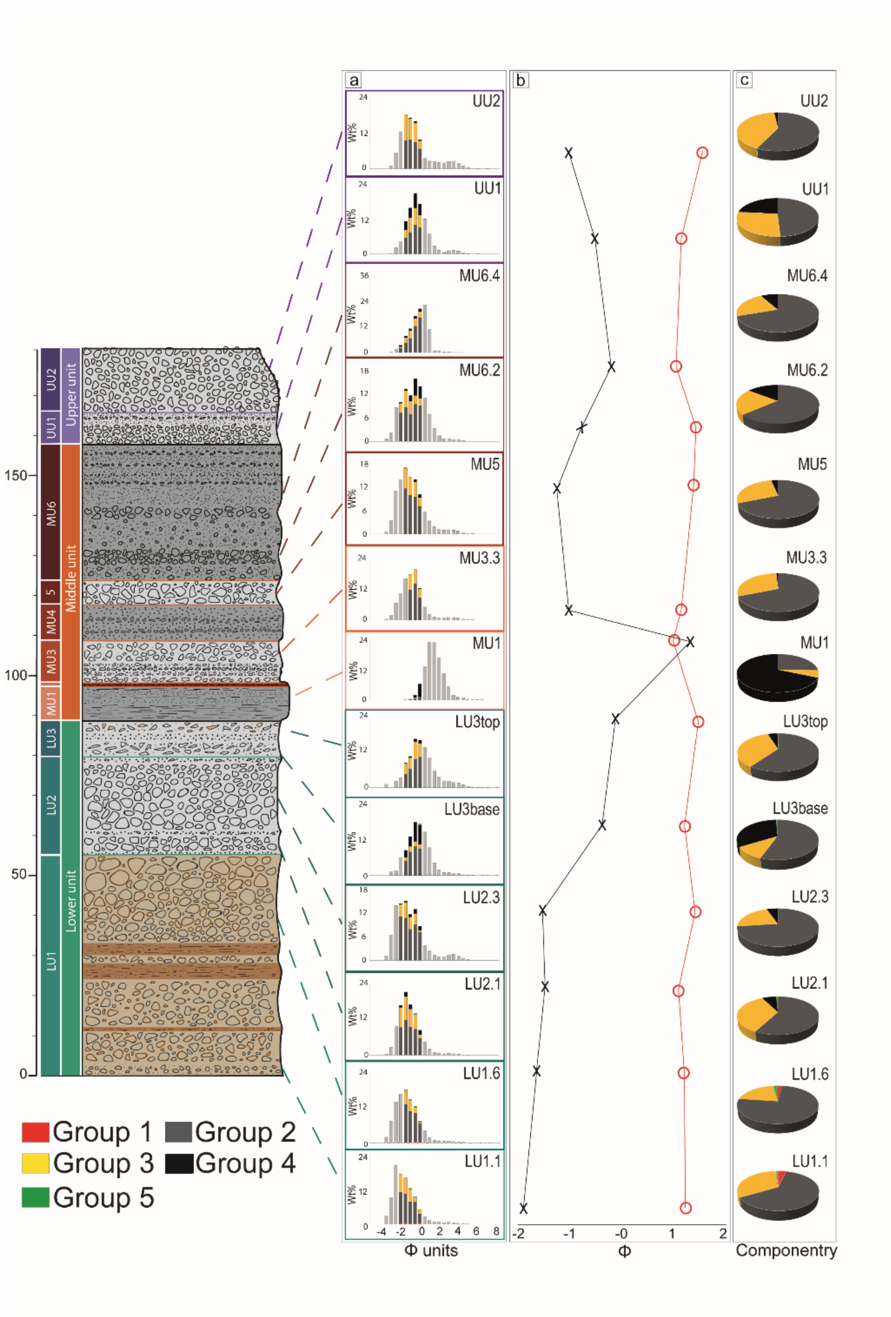

Fig. 2 Stratigraphic section of the tephra sequence at LP35, ~1 km SW of the vent area (adapted from Bonadonna et al. 2022) correlated with a) local grain-size distribution b) Mdϕ and σϕ and c) pie diagrams that show the relative abundance of the five components for representative tephra layers (see main text for componentry grouping). Indentation of the stratigraphic column increases with decreasing grain-size. Note that sample MU1 was taken at location LP16

Component analysis was conducted on the coarsest (−2ϕ to 0ϕ) grain-size fractions of samples from LP35; five different groups of juvenile fragments and a group of lithic clasts could be identified (Fig. 3): (i) juvenile, spongy, highly vesicular clasts, (ii) juvenile, glassy, variably vesicular clasts, (iii) juvenile, elongated, variably vesicular clasts (iv) juvenile scoria with dense groundmass and isolated vesicles, (v) free crystals and (vi) lithics.

- Group 1: low-crystallinity, microlite-poor clasts that show a wide range on vesicle shapes and sizes. They are characterized by irregular outer surfaces due to the presence of broken and thin bubble septa. The clasts appear "spongy", highly vesicular and generally translucent with a light colour (brown; Fig. 3a). They are found only in the first erupted products of the Lower Unit (layers LU1.1 and LU1.6) and are absent in the Middle and Upper Unit.
- Group 2: clasts characterized by variable morphology, texture, and vesicularity (Fig. 3b). They show a higher crystallinity than Group 1 clasts and differ mainly in the range and proportions of vesicle sizes. Some clasts show nearly equidimensional shape and the outer surface is generally smooth, glassy and fluidal; other clasts, which are highly vesicular, are characterized by a heterogeneous vesicle distribution, rough outer surface and an irregular morphology. The Group 2 clast type constitutes the dominant component in all three units; they are most abundant in the Lower Unit (between 55-75%), followed by the Middle Unit (25-69%) and the Upper Unit (49-57%).
- Group 3: clasts show the widest vesicles size range due to the coexistence of large, irregular/elongated, and small, almost spherical bubbles (Fig. 3c). The outer surface is generally smooth and glassy, and the shape of the clasts is contorted, fluidal, and elongated (rod-like). Occasionally, the surface displays more irregular outlines due to the presence of torn and broken vesicles. Clasts have generally translucent dark colour, but some vesicular clasts exhibit lighter colours. These clasts occur in different

proportions in all three tephra units; they are more abundant in the Upper Unit (between 27-41%), followed by the Lower Unit (10-35%) and the Middle Unit (6-30%).

- Group 4: clasts are juvenile and show a crystalline and microlite-rich groundmass, in contrast to the glassy, almost microlite-free nature of Group 1. Vesicles are isolated and variable in size and shape (e.g., round, flattened and deformed) and the clasts generally appear scoriaceous with equidimensional and subspherical morphologies and a dense groundmass. Sometimes the clasts are blocky and the outer surface is covered with a reddish colour. The clasts of this group are most abundant in the Middle Unit (68% to 1%), where they represent the dominant component for MU1. However, they occur also in the Upper Unit (23% to 2%) and the Lower Unit (32% to 4%).
- Group 5: millimetric to sub-millimetric crystals of euhedral pyroxene and, in smaller amounts, olivine crystals. They are present in varying amounts only in the erupted products of the Lower Unit (between 1 % and 2 %).
- Group 6: lithic material is generally characterized by altered and strongly oxidised, scoriaceous clasts. They display predominantly rounded morphologies and are often brown/reddish in colour. Lithic material generally shows abundances below the detection limit (<<0.04 g) and is found sporadically in all three units.

Analysing the variations of the components along the stratigraphic sequence (Fig. 2a, c), we observe that the LU1.1 and LU1.6 sublayers are characterized by the presence of up to 4% of the highly vesicular Group 1 clasts and 1-2 % of free crystals . In both sublayers, Group 2 clasts represent the dominant component (63.0% in LU1.1 and 75.1% in LU1.6). Group 3 clasts follow in terms of abundance (32.2% and 20.7% for LU1.1 and LU1.6, respectively). In LU2, Group 1 clasts disappear completely, while scoriaceous Group 4 clasts constitutes 6.6% in LU2.1 and 5.3% in LU2.3. Group 2 clasts remain the dominant component (57.8% in LU2.1 and 72.9% in LU2.3), followed by Group 3 clasts, with abundances of 34.7% in LU2.1 and

21.7% in LU2.3. Group 4 clasts increase significantly in the final products of the Lower Sequence (LU3) with abundances of 32.8%, and become the dominant component in the first products of the Middle Unit, (in MU1, 68.4%). It is worthy to highlight that MU1 has grain-sizes >>0 ϕ, which is why only a minor part was characterized in terms of componentry (cf. Fig. 2a).

Starting from MU3.3, the proportion of Group 2 increases again (68.9%), while Group 4 clasts decrease significantly, representing only 0.9% of the components, while they increase again in the last sublayers of the Middle Unit (MU6.2 and MU6.4) reaching values of 14.5%. In these sublayers, the dominant component remains Group 2 clasts, with abundances of 63.5% in MU6.2 and 70.0% in MU6.4, followed by Group 3 clasts, which constitute 22.0% in both sublayers. The last emitted products (layers UU1 and UU2) are marked by a predominance of Group 2 clasts, with abundances of 49.1% in UU1 and 57.1% in UU2. Group 4 clasts represent a significant component in UU1 (23.4%) but decrease dramatically in UU2 to 1.8%. Group 3 clasts remain abundant (27.4% in UU1 and 41.1% in UU2).

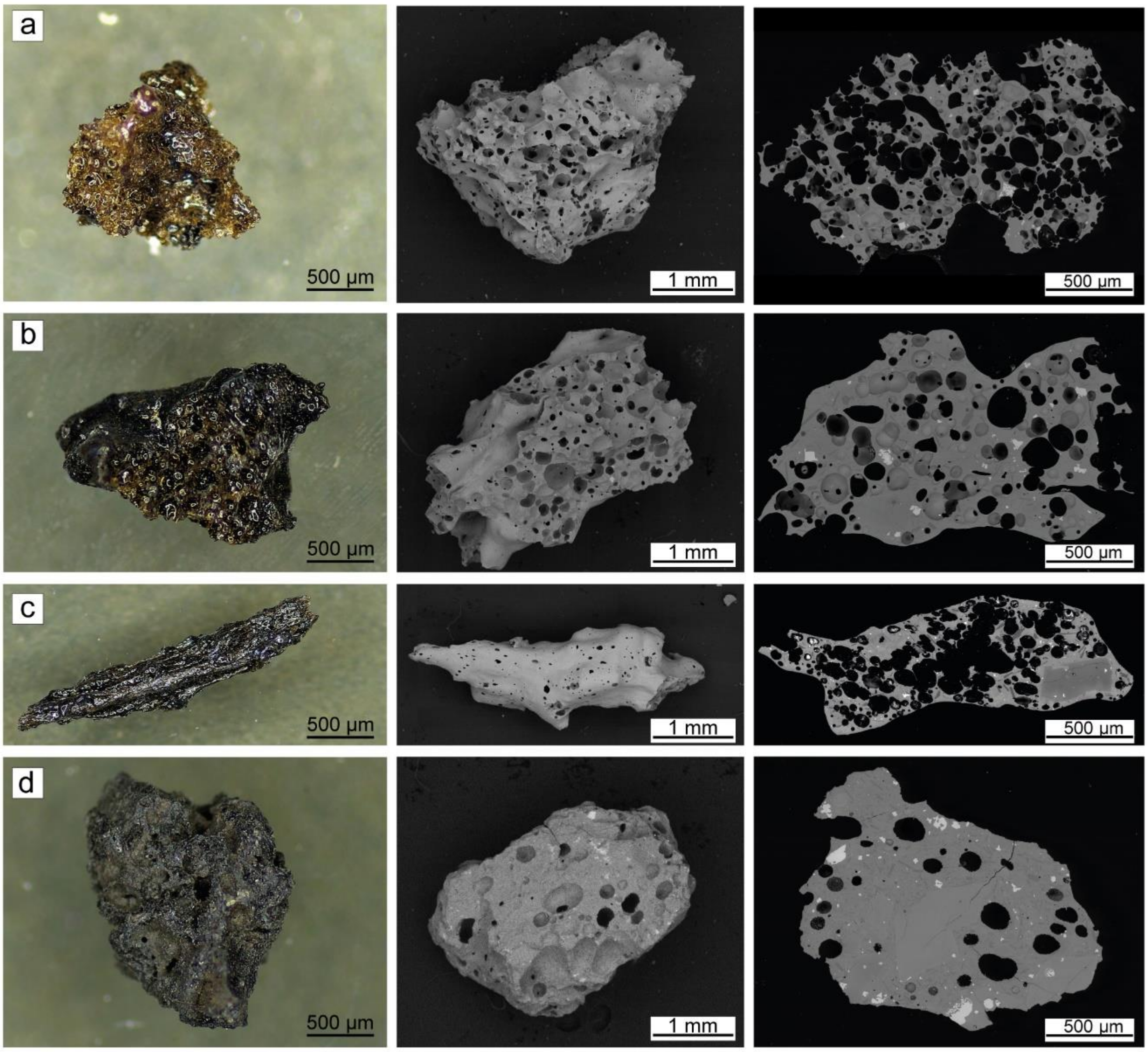

Fig. 3 Images of juvenile (a) spongy clasts (Group 1); (b) glassy, variably vesicular (Group 2); (c) elongated, variably vesicular (Group 3); (d) scoria with dense groundmass and isolated vesicles (Group 4). Stereomicroscope images of the clasts on the *left*, SEM-SE images in the *center* and SEM-BSE images on the *right*

3.2 Bulk density of juvenile clasts

Density measurements were performed on centimeter-sized clasts from selected coarse layers (100 clasts per each layer) that are representative of the whole eruptive sequence at both key sections LP35 and LP27. Overall, density values range from 573 to 2428 kg/m^3. At LP35, the density distributions show generally unimodal trends (Fig. 4). LU shows the lowest density modes of the whole sequence, ranging from 573 to 2335 kg/m^3 with modes decreasing from

1021 kg/m^3 in LU1.1, to 894 kg/m^3 for LU1.2, 867 kg/m^3 for LU1.6 and 866 kg/m^3 for LU2.3. LU3 shows a slight density increase with a bimodal distribution, highlighting a primary mode at 1082 kg/m^3 and a secondary mode at 1620 kg/m^3. Following LU3, modes increase slightly to ~1070 kg/m^3 for MU3 and MU5 and remain constant during UU.

At LP27, density distributions show generally bimodal trends, with the exception of layers LU2 and UU, which show unimodal distributions (Fig. 4). LU density measurements show the lowest values and range from 634 to 2325 kg/m^3 with a marked density increase from 863 kg/m^3 in LU1 to1223 kg/m^3 in LU3. Similar to LP35, LU3 displays a secondary high density mode at 1840 kg/m^3. In the Middle Unit, the density values are generally higher than in LU but decrease linearly from MU3 to MU5. The density distributions are bimodal with modes at 1071 and 1617 kg/m^3 for MU3 and 1047 and 1417 kg/m^3 for MU5. In the Upper Unit, density measurements indicate a mode at 1073 kg/m^3 (Fig. 4).

Density values were converted to vesicularity using a DRE = 2700 kg/m^3 and following Houghton and Wilson (1989). At both locations, the highest values occur in the first layers of the sequences (LU1.1, LU1.6 and LU2.3 for LP35 and LU1, LU2 for LP27), with a mode at 58.7%. In both deposits, a decrease in vesicularity is observed at the end of the Lower Unit (layer LU3) and throughout the Middle Unit, with values ranging from 50.0 to 53.2%. A new increase in vesicularity is observed in the final products of the eruption (layer UU2 for LP35 and UU for LP27) with a mode at 54.0%.

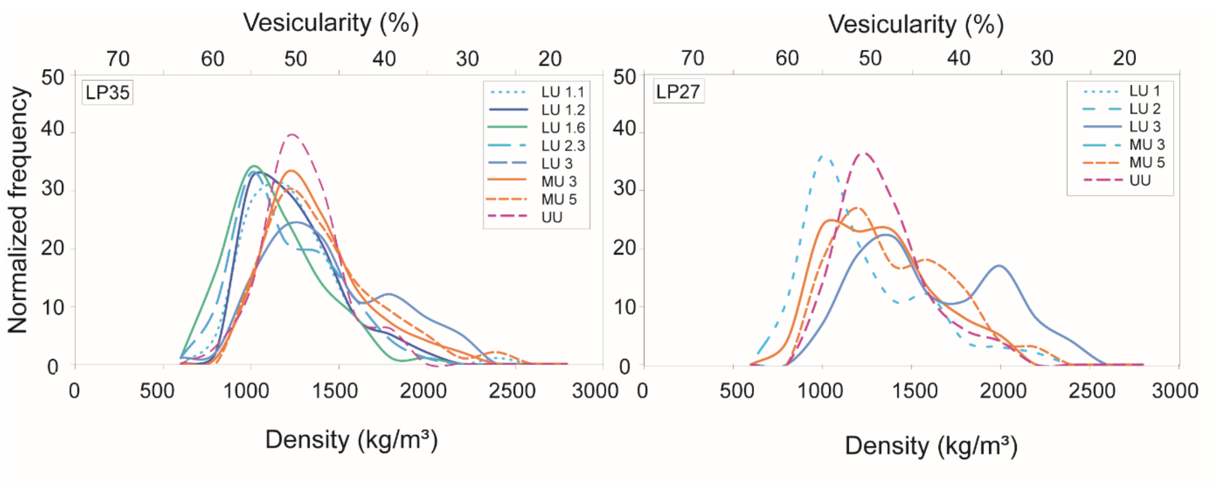

Fig. 4 Vesicularity and density distributions for juvenile vesicular fragments collected from selected layers at LP35 (~1 km SW of the vent) and at LP27 (~1 km NE of the vent)

3.3 Morphological and textural ash characterisation

Morphological and textural characteristics are described below for the main juvenile groups identified through componentry analysis. Particle morphology is described in terms of shape parameters such as solidity, convexity, axial ellipse ratios and concavity index (CI) (Fig. 5; Table S1). Groundmass textures are described in terms of vesicle and phenocryst content, and vesicle size (Table S2).

Group 1 clasts show predominantly irregular morphology and rough external surfaces, related to the presence of large internal vesicles reflecting their highly 'spongy' character (Fig.5). The average 2D vesicularity is high, at 68.9% (σ= 2.2) and the N_V^m average value is 33.9·× 10^6 cm^{-3} (σ=7.3). The diameters of vesicles vary between 0.005 and 0.317 mm at the base of the stratigraphic succession, decreasing regularly upward. Bubbles are generally irregular in shape, but small spherical vesicles, sometimes elongated, are also present. Vesicle volume distributions (VVDs) are polymodal, with multiple distinct modes and VSD plots (ln population density versus size) show curved and concave upward distributions for the smaller size classes. Phenocrysts are absent, while microlite content is variable (Fig. 6 example clast 6B).

Group 2 clasts show the largest range of variability in morphological parameters, indicating clasts with smooth and rough surfaces, determined by the presence of vesicles of varying size, and with morphologies that range from nearly equidimensional (axial ratio values close to 1) to irregular (Fig.5). They show a wide range of 2D vesicularity, ranging from 15.0 to 56.0% (average value 35.8%, σ=10.4) and an average N_V^m of 19.8·× 10^6 cm^{-3} (σ = 18.0). Vesicle diameter varies between 0.0021 and 0.335 mm. Bubble shape is variable; large bubbles sometimes show irregular shapes, while small bubbles are generally spherical, sometimes elongated. Vesicle volume distributions (VVDs) are polymodal, with two or three distinct modes; in some samples, distributions are positively towards the largest size classes. VSD graphs show curved and concave upward distributions for the smaller size classes. The content of phenocrysts varies from 2 to 18% (Fig. 6, example clast 35T).

Group 3 clasts are marked by smooth to rough outer surfaces, as well as predominantly irregular morphologies. This group shows distinguished low axial ratio values (0.25 to 0.46; Fig. 5c), in line with the macroscopically observed elongated morphologies. The average vesicularity is 17.3 % (σ=11.9) and the average N_V^m has a value of 26.9·× 10^6 cm^{-3} (σ=30.8). The vesicle diameter varies between 0.003 and 0.042 mm at the base of the stratigraphic succession, decreasing regularly upward. Clasts are characterized by the coexistence of large, flattened, elongated bubbles and small, rounded, nearly spherical bubbles (Fig. S3, example of 37S clast). Vesicle volume distributions (VVDs) are polymodal and the phenocryst content is between 8 and 19% (Fig. 6 example clast 13H).

Group 4 clasts show morphological parameters indicative of predominantly dense clasts with spherical/regular morphologies and smooth to rough outer surfaces (Fig. 5). The average 2D vesicularity is 22.0% (σ=8.37) and the average value of N_V^m is 20.90·× 10^6 cm^{-3} (σ=20.90). Vesicle diameter varies between 0.004 and 0.364 mm, increasing toward the top of the succession. The bubbles are often isolated with irregular shapes reflecting crystal growth on the bubble walls. The phenocryst content is between 2 and 47%. VVD graphs show a polymodal distribution with modes generally clustering in the larger size classes (Fig. 6 example clast 34 S). Both morphological and textural characteristics vary within individual layers and show consistent trends along the stratigraphic sequence.

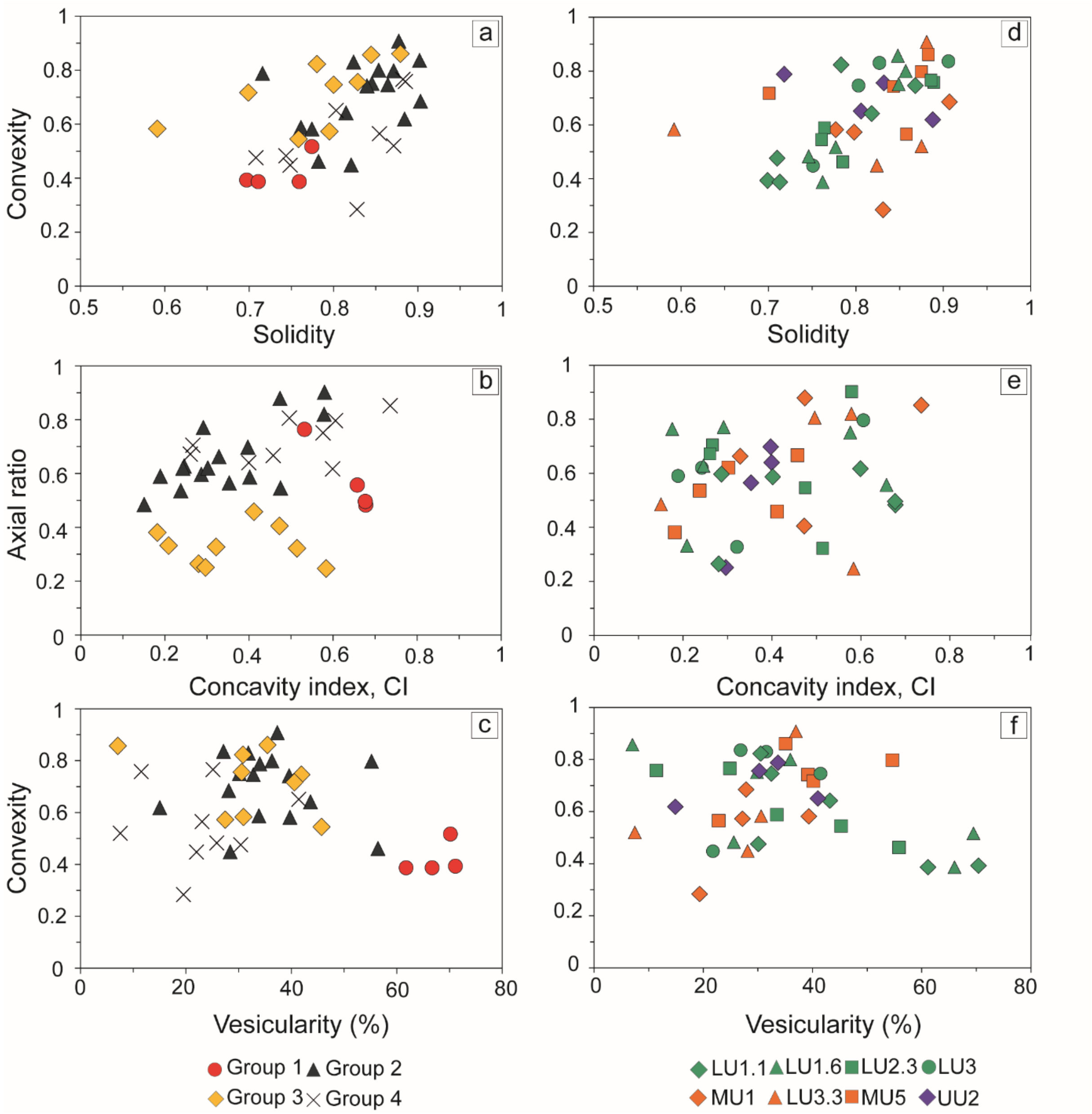

Fig. 5 Ash characterization by shape analysis. Solidity versus Convexity, Concavity index (CI) versus Axial ratio and Vesicularity versus Convexity for each group identified (a, b and c) and along the eruptive sequence (d, e, f)

The morphological and textural features of the studied units can be described by grouping the analysed clasts in the respective tephra layers along the sequence. Within the Lower Unit, the clasts generally show high solidity values (0.70 to 0.87) and a wide range in convexity values (0.39 to 0.82) indicating the presence of predominantly vesicular particles with smooth to rough outer surfaces (Fig. 5). Axial ratios are the lowest in LU1.1, highlighting highly irregular clast morphologies. This conforms with high proportions of elongated clast morphologies (Group 3) as indicated from componentry. The average 2D vesicularity decreases almost linearly from LU1.1 (41.8%, σ=15.5) to LU3 (30.7%, σ=7.3; Fig. 9b), while average N_V^m values are overall lower than those of the other units (13.8×10^6 cm^{-3}, σ=11.9; Fig. 9a). The clasts are marked by small vesicles that tend to reduce in diameter upward (from 0.005-0.317 mm in LU1.1 to 0.004-0.269 mm in LU3. Overall, in LU, morphological and textural characteristics vary only slightly between pyroclasts of different componentry classes.

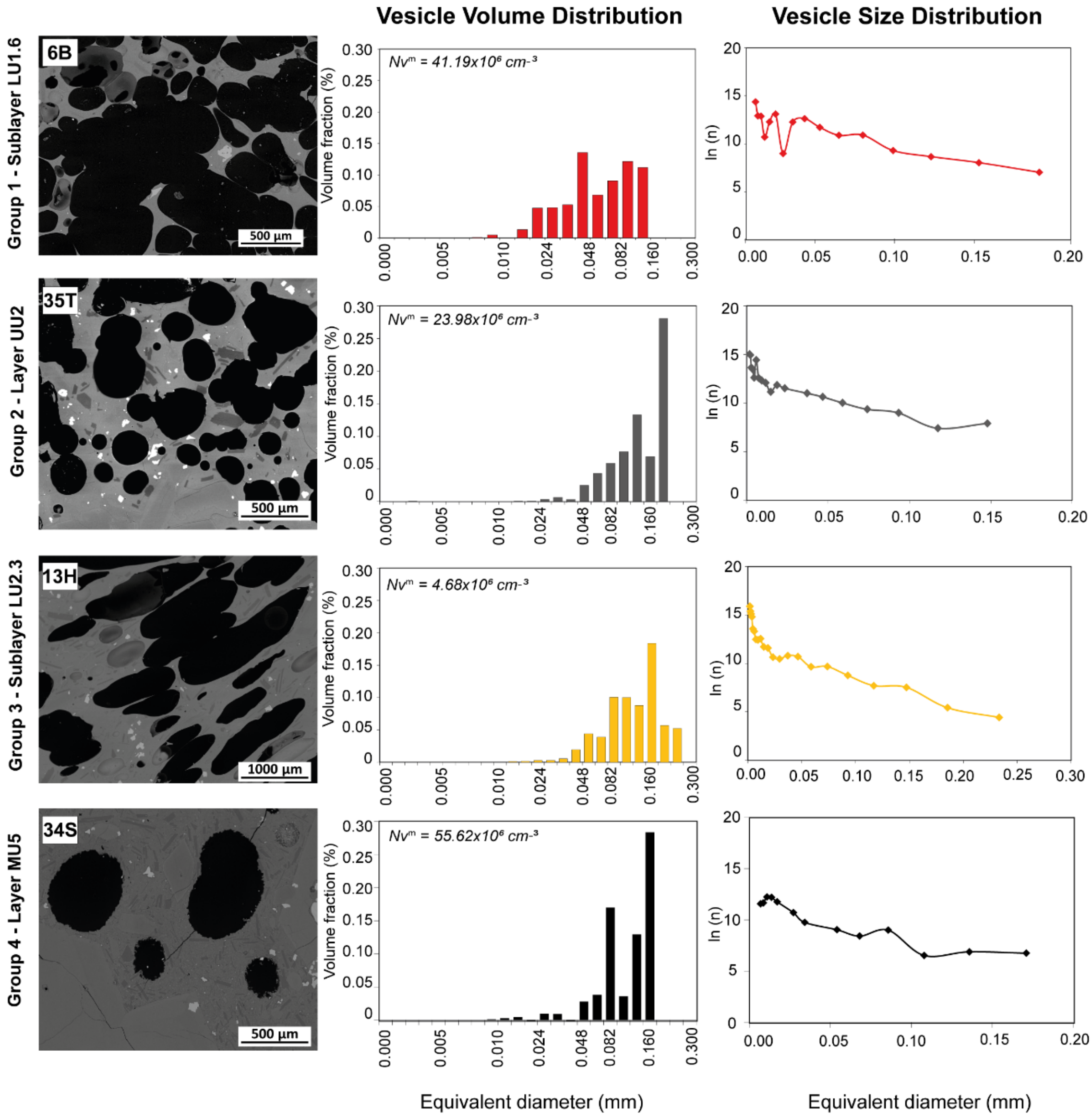

Fig. 6 BSE images of the bubble texture, Vesicle Volume Distributions (VVD) and Vesicle Size Distribution (VSD) of a clast as an example for each identified group

Within the Middle Unit, clasts show greater variability in the parameters of solidity (0.59 to 0.91) and convexity (0.28 to 0.91), which overall are higher than the clasts belonging to the Lower Unit and indicate the presence of denser clasts with more regular morphologies (Fig. 5). A pronounced decrease in convexity can be observed for MU1, concomitant with a sharp increase in axial ratios, indicating more equidimensional clast shapes (Fig. 5d). The average 2D vesicularity in MU1 is the lowest in the entire sequence (28.1%; Fig. 9b), however, accompanied by an increase in N_V^m values (N_V^m= 42.0×10^6 cm^{-3}; Fig. 9a). Compared with MU1, from MU3.3 until the end of the Middle Unit, image vesicularity increases (average value for MU3 and MU5 of 38.5%, σ=9.4) and N_V^m values decreases (30.7×10^6 cm^{-3}; σ=19.9, Fig. 9). MU5 display a decrease in vesicle size, and clasts have low axial ratios (0.39 to 0.67) consistent with their elongated morphologies (Fig. 5).

Finally, in the Upper Unit, the clasts show overall high values of solidity and convexity (average value 0.81 and 0.70, respectively) which indicate the presence of predominantly dense fragments with smooth outer surfaces, which is also confirmed by the low CI values (0.3 to 0.40; Fig. 5). Highly variable axial ratio values (0.26 to 0.70) indicate the coexistence of irregular and subspherical clasts within the same layer. The 2D vesicularity values are lower (average value 30.3%, σ=9.6 Fig. 9a) while the number of vesicles per clast increases (average value N_V^m of 47.9 × 10^6 cm^{-3}, σ=33.6; Fig. 9b). This increase in N_V^m seems to contradict the decrease in image vesicularity with eruption progression (Fig. 9). However, these observations can be reconciled by the observation that the smallest vesicle sizes also decrease with eruption progression (Fig. 5e). Thus, vesicularity is increasingly composed by smaller vesicles, that contributes little area/volume to the overall vesicularity, coherent with the observed declining image vesicularity (i.e., UU). Comparing VVDs from UU to those from LU, the former highlight a large spread and are skewed towards large sizes. At the same time, the presence of small vesicles with 0.002 mm is also evident (Fig. 6).

3.4 Matrix glass analyses

Matrix glass analysis was performed on the different types of ash fragments from all the studied layers and sub-layers (Table S3). Major element values for most samples cluster in a narrow range within the tephrite to basanite field on a total alkali vs. silica plot (TAS), with values that range between 43.2 and 46.5 wt.% of SiO_2 and between 6.68 and 8.5 wt.%. of total alkali (Na_2O + K_2O). All samples are tightly clustered between 8.5 and 11.64 wt.% of CaO, 3.55 and 4.71 wt.% of MgO, 9.24 and 12.25 wt.% of FeO and 15.20 and 17.15 wt.% of Al_2O_3 (Figs. 7,8; Table S3).

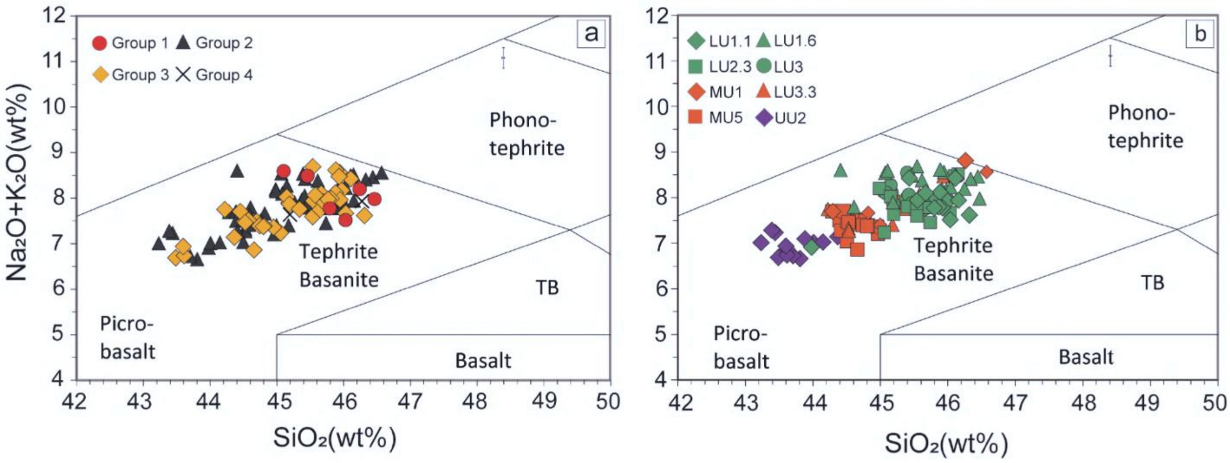

Fig. 7 Total alkali vs. silica diagram (TAS) showing matrix glass composition for volcanic ash from the Tajogaite eruption. a) TAS for the main componentry groups show a compositional range between tephrite and basanite, and the clasts in Group 1 show a narrow variability. b) variability of clasts composition along the eruptive sequence highlight a gradual decrease in SiO_2 and alkali total with eruption progression

When considering the different groups, Group 1 clasts show narrow variability for SiO_2 ranging from 45.1 to 46.4 wt.% (σ= 0.50), total alkali (Na_2O + K_2O) between 7.5 and 8.5 wt.% (σ= 0.41), and slight variations of FeO and MgO between 9.6 and 10.1 wt.% and 3.7 and 4 wt.%, respectively (Fig. 8). Group 2 clasts show greater variability than Group 1 and generally lower SiO_2 contents (43.2 –46.5 wt.%, σ=0.83). The content of total alkali varies between 6.6 and 8.6 wt.% (σ=0.52), while FeO ranges between 9.8 and 12.2 wt.%, MgO between 3.6 and 4.5 wt.% and CaO between 8.9 and 11.4 wt.% (Fig. 8). Group 3 clasts show variations of SiO_2 between 43.4 and 46.3 wt.% (σ=0.76) and Na_2O + K_2O between 6.6 and 8.6 wt.% (σ=0.50). Variations are also observed in the content of FeO (between 9.2 and 12 wt.%), MgO (between 3.5 and 4.7 wt.%) and CaO (between 8.9 and 11.6 wt.%, Fig. 8). Group 4 clasts show a very crystalline groundmass, which is why only two samples were analyzed for this group (Fig. 8). Irrespective of the componentry class, with the exception of Group 1, all clasts show a wide variability, covering the entire compositional range.

Trends observed along the eruptive sequence witness increasingly mafic compositions. In particular, the clasts ejected during the early eruptive phases (layers LU1.1, LU1.6, LU2.3 and LU3) show predominantly tephritic compositions, with higher SiO_2 and total alkali (Na_2O + K_2O) values and lower FeO, MgO and CaO, while the clasts ejected in the mid-to-late phases of the eruption (layers MU1, MU3. 3, MU5 and UU2) shift towards basanitic compositions, showing overall lower contents of SiO_2 and total alkali and higher concentrations of FeO, CaO and MgO (Figs. 7, 8).

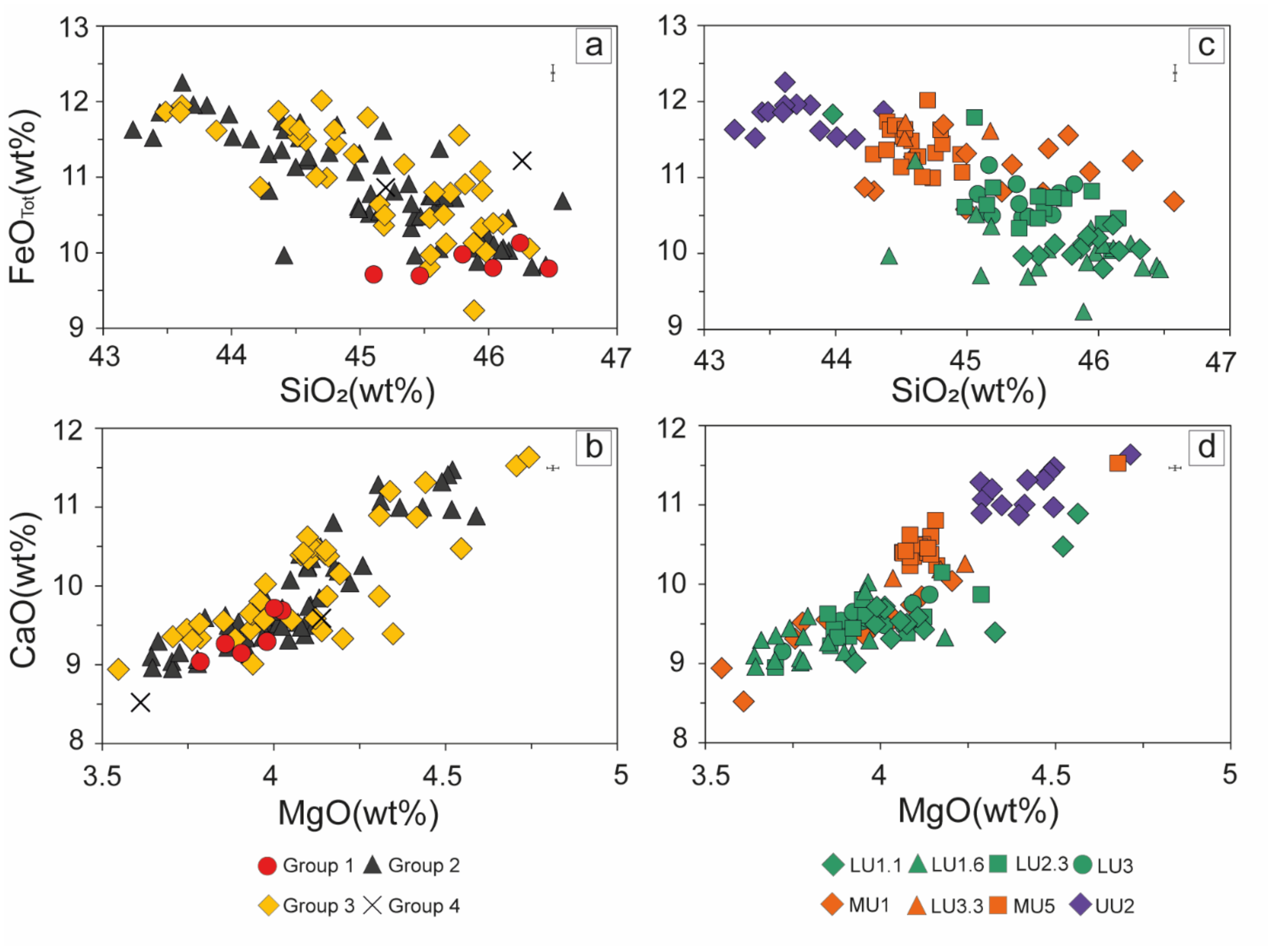

Fig. 8 Variation diagrams for selected major element oxides for the glassy matrix of volcanic ash from the Tajogaite eruption; FeO_{Tot} vs SiO_2 for individual componentry classes and along the eruptive sequence (a and c respectively) and CaO vs MgO for each group identified and along the eruptive sequence (b and d respectively). Note that the clasts of Group 1 show a narrow range of variability with low concentrations of SiO_2, FeOTot, MgO and CaO, while the products ejected in the mid-to late stages show higher values of SiO_2, FeOTot, MgO and CaO

4. DISCUSSION

4.1 Syn-eruptive tephra variability

The simultaneous explosive and effusive activity that characterizes hybrid eruptions can occur when magma separates into vertical and lateral accumulation zones in the conduit in which gas and liquid components are not uniformly distributed (Pioli et al. 2008, 2009; Taddeucci et al. 2023). In this case, outgassed magma preferentially ascends from the lateral branches of the conduit, giving rise to effusive or low-intensity activity, while gas-rich magma rises from the vertical sections, feeding explosive activity. This process, which has already been advocated to describe similar eruptions (e.g., Parìcutin (Pioli et al. 2008); Etna (Taddeucci et al. 2002; 2004)) has been invoked also for the Tajogaite eruption (Bonadonna et al. 2022; Taddeucci et al. 2023) to explain the presence of low-viscosity magma which initially ascended from relatively immature conduits and later favoured the separation into vertical and lateral branches near the base of the cone. This is also suggested by detailed pre- and syn-eruptive seismic data (D'Auria et al. 2022; Del Fresno et al. 2023), which identify multiple interconnected magma batches in which magma ascended from different depths and with different velocities. In simultaneously active multi-vent dynamics, it is common to observe the formation of juvenile material that shows different features depending on the changes that occur in the magmatic system and during magma ascent. A significant aspect also concerns the geometry of volcanic conduits; particular geometries, such as constrictions or branching of conduits, may be responsible for the segregation of magma, affecting outgassing and fragmentation processes during ascent (Pioli et al. 2009, 2017). In this section, we focus on the syn-eruptive variability of the juvenile material ejected during explosive activity, to propose possible conduit dynamics. The analyses have identified four main groups of juvenile clasts ejected during the eruption and found in different proportions within individual layers/pulses. In line with recent experimental studies (Arzilli et al. 2019), we suggest that the highly vesicular clasts, identified as Group 1 (Fig. 3a), formed in the hottest, more insulated central zones of the conduits. In these zones, portions of volatile-rich magma ascended at high velocities. High P-T gradients favour volatile overpressure conditions (Sparks 2003; Taddeucci et al. 2004; Pioli et al. 2009). Fragmentation in the central zone of the conduits is efficient (Kueppers et al. 2006) and results in the ejection of highly vesicular clasts sometimes marked by collapse and coalescence of bubbles (Fig. 6, example of clast 6B). The variably vesicular clasts of Group 2 (Fig. 3b) represent the dominant component of the entire eruption and display a great variability in textural and morphological parameters even within individual layers (Fig. 5a,b,c). The vesicles show collapse and coalescence phenomena (Fig. 6, clast 35T). These clasts may have formed in intermediate zones of the conduits, which are marked by variable P-T gradients. In these regions, magma may be susceptible to variations in ascent rates and magma/gas ratios, contributing to the formation of clasts with variable textural and morphological features. As suggested by Houghton et al. (2004), timing also plays a key role in the features of the ejected clasts. The more vesicular and less vesicular juvenile material was probably influenced by the different timing of accumulation and ascent within the conduits. The elongated and variably vesicular clasts of Group 3 (Fig. 3c) show fluid, stretched morphologies and low axial ratio values (Fig. 5b). Vesicles are both elongated, deformed and connected (Fig. 6, clast 13H) and spherical and isolated (example of clast in Fig. 3c), suggesting a genesis in narrower areas of the conduits (e.g., along conduit walls) during rapid magma ascent. In these areas, the magma is subjected to high pressures and increased strain, which causes external deformation of the clasts and of the internal vesicles in some cases (Wright and Weinberg et al. 2009), while in others high magma fluidity allows bubble relaxation, hence resulting in spherical vesicles (Pistolesi et al. 2015). Finally, the scoriaceous clasts of Group 4 (Figs. 3d and 6, example of clast 34S), that are characterized by lower vesicularity, higher crystallinity and a predominantly subspherical shape likely represent colder, lateral sections of the conduits. In these zones, where portions of magma accumulate and rise at lower velocities, the magma is partially outgassed and the fragmentation efficiency is reduced (D'Oriano et al. 2022). Instead, crystallization processes are favored, in agreement with less vesicular, denser clasts.

Deposits always represent the overall signature of the eruption at any given time, with limited opportunities to resolve "individual" explosions. We suggest that the variability in pyroclast components and their morphological-textual characteristics can be ascribed to their origin in different portions of the conduit system, that are active and ejected simultaneously. Both lateral heterogeneities within the same conduit as well as ejection from separate conduits can potentially explain the observed variability, considering short-term spatial variations in flow dynamics, vent geometry, magma ascent rates, and magma/gas ratios (Bonadonna et al. 2023; Taddeucci et al. 2023). In turn, these parameters significantly affect magma outgassing and fragmentation processes and therefore the observed eruption dynamics.

4.2 Temporal variability of the juvenile material

Temporal variations in the characteristics of ejected juvenile material are indicative of explosive activity marked by varying dynamics in time. This is in agreement with detailed seismic and geochemical studies (Dayton et al. 2023, 2024; Ubide et al. 2023; Zanon et al. 2024) suggesting the Tajogaite eruption has been fed by multiple pulses of magma having different characteristics, and which has ascended from distinct accumulation zones at different depths. These data are discussed here to better understand the eruption dynamics. In agreement with the sedimentological studies by Bonadonna et al. (2022) and Romero et al. (2022), three main eruptive phases characterize the Tajogaite eruption, during which minor changes in eruptive activity occurred over shorter time scales.

Phase I (LU1 to LU3; 19 Sept to 10 Oct). The strong homogeneity in the physical and geochemical characteristics of the sublayers representing the first 8 days of eruptive activity (LU1.1 and LU1.6) suggests that this initial phase is guided by linear and homogeneous processes, likely related to a more evolved magma that was emplaced into a shallow reservoir in the weeks prior to eruption start (D’Auria et al. 2022; Del Fresno et al. 2023; Zanon et al. 2024). Textural characteristics vary only slightly between different componentry types but analysis of ejected material suggests that the initial activity remained of high intensity, marked by distinct pulses of magma that produced mid- and high-vesicular clasts of Groups 1, 2 and 3. From Layer LU2 (LU2.1, LU2.3), the overall grain-size of the clasts decreases, and Group 1 disappears completely. Instead, Group 4 clasts are found (Fig. 2), which present few isolated vesicles (low vesicularity) and higher crystallinity (Fig. S1 example of 19G clast). The average vesicularity of the clasts increases, while the number of bubbles per unit volume of melt decreases (N_V^m, Fig. 9a). A first evident change in pyroclast characteristics appears during LU3; specifically, an increase in overall density and the observed secondary high-density component indicate staggering and crystallisation. This change in eruptive style also favours a slightly different degassing history for the melt, as witnessed by increasing proportions of the scoriaceous Group 4 clasts. The change is probably related to a decrease in ascent velocities and/or gas supply with gas-poor magma ascending at lower velocities, favouring the formation of more crystalline and denser juvenile material. The magma that fed Phase I shows evolved compositions that falls within the tephritic range (Fig. 7) and shows limited variability between different components. However, with eruption progression, slight variations in magma composition are observed, indicating increasingly more primitive tephritic-basanitic compositions (Figs. 7, 8 and 9c). Subsequently to the ejection of the more evolved, previously emplaced magma, new pulses of more primitive magma have ascended from deeper zones, mixing with the more evolved magma batches (Dayton et al. 2023, 2024; De Luca et al. 2022; Ubide et al. 2023; Zanon et al. 2024).

Phase II (MU1 to MU6; 10 Oct to 25 Nov). While composition remains largely similar with LU (Fig. 9c), physical parameters of the ejected pyroclasts change, involving a sudden decrease in grain-size, the predominance of the scoriaceous Group 4 component in the initial MU1 (Figs. 2b, c), as well as a sudden decrease in vesicle size. Crystallization is more extensive with abundant formation of dense clasts. These features point towards a less efficient magmatic fragmentation (Kueppers et al. 2006), in agreement with decreasing lava discharge rates and changing eruptive conditions (Bonadonna et al. 2022). This phase was potentially influenced by slower magma transfer rates at depth (cf. Zanon et al. 2024). Consequently, observations suggest that the fine grain-size observed in MU is not ascribed to more efficient magma fragmentation, but rather to changing conduit dynamics which generated a different eruptive style. From the MU3 layer until the end of Phase II (MU3.3, MU5, MU6.2 and MU6.4), componentry data show that Group 2 clasts return to be the dominant component, while Group 4 clasts are the least abundant component (Fig. 2). Vesicularity values increase with the presence of bubbles of variable size, sometimes affected by coalescence phenomena, and a decrease of the average N_V^m values (Fig. 9). Physical characteristics indicate that bubble growth/coalescence had an important influence and contribution to overall vesicularity, likely due to increased magma fluidity. Convexity increases with vesicularity, suggesting that for these units the more vesicular pyroclasts display a regular, dense morphology (Liu et al. 2015), related to the presence of fluidal and glassy outer surfaces (Fig. S2 example of 28N clast). The variations in the proportions of juvenile material emitted may be related to different magma pockets at depth (Cashman et al. 2017; Zanon et al. 2024). Magma batches that fed Phase II have less evolved compositions (Figs. 7 and 9c). This is in agreement with Ubide et al. (2023) and Zanon et al. (2024) who indicated that after the depletion of the more superficial accumulation zones that fed Phase I, deeper and more primitive magma batches were ejected. Following MU1, magma recharge occurred at variable rates and from variable depths (Zanon et al. 2024), feeding the pulsatory activity observed during MU (Taddeucci et al. 2023; Bonadonna et al. 2022; 2023). In particular, variations of ur occurred during the sedimentation of the MU, changing from puffs of ash-poor gas to violent Strombolian activity (Bonadonna et al. 2022, 2023). Benito et al. (2023) analysed temporal variations of geophysical parameters (such as seismicity and deformation) and found significant changes in seismic intensity in November, which could correspond to variations in eruptive style during MU sedimentation, in agreement with our study.

Phase III (UU1 to UU2; time 25 Nov to 13 Dec). During this phase, both the chemical compositions and physical parameters of the ejected pyroclasts show significant changes. Medium to high vesicularity components of Group 2 and Group 3 are predominant while scoriaceous clasts of Group 4 are found to a small proportion (Fig. 2). Juvenile fragments present N_V^m values, that are highly variable between different component types comprising both small vesicles as well as larger vesicles that sometimes exhibit coalescence and collapse phenomena (Fig. 5, example clast 35T). Overall, this phase shows the highest average N_V^m values of the entire sequence (Fig. 9a), while vesicularity is lower than for the other phases (Fig. 9). Morphological parameters indicate the presence of dense clasts with smooth outer surface, while textural analysis testifies moderate internal vesicularity (Figs. 4 and 5). This, is in line with high proportions of the fluid and elongated clasts of Group 3 and more primitive glass compositions and suggests overall high magma fluidity and low viscosity.

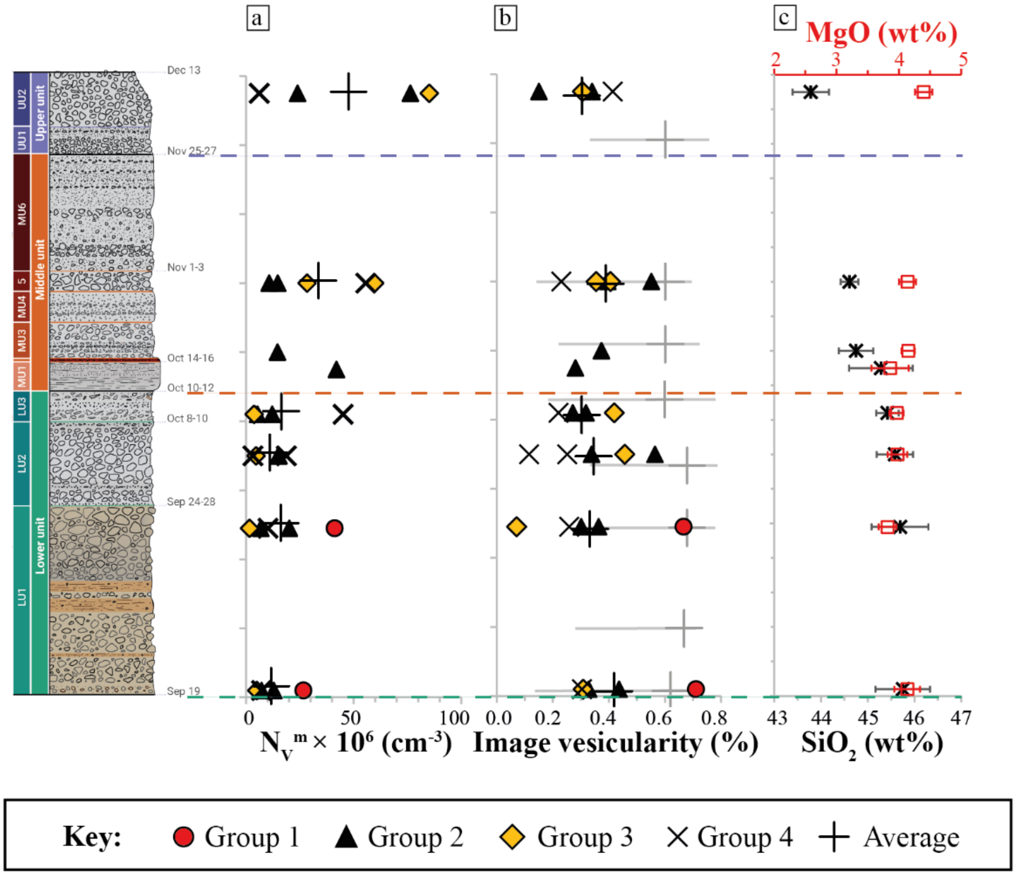

Fig. 9 (a) N_V^m, number of bubbles per unit volume (cm^{-3}) for different componentry groups. Layer-average is marked by plus sign (b) Image vesicularity (%) for different componentry groups derived from image analysis. Layer average is marked by plus sign. For comparison vesicularity (%) derived from density analyses is reported in grey: plus signs mark the primary mode, while the distribution range is marked by the grey line. (c) SiO_2 and MgO compositions of the analyzed clasts in the analysed layers and sublayers are shown with a black star and a red square, respectively

In agreement with previous studies (Ubide et al. 2023; Dayton et al. 2023, 2024; Zanon et al. 2024), we suggest that these final batches probably ascended in a shorter time from deeper accumulation zones. The more primitive, tephritic-basanitic chemical compositions of the clasts (Figs. 7, 8 and 9c) suggests a provenance from relatively deeper zones of the magmatic system, and the significant abundance of elongated Group 3 clasts may be indicative of rapid ascent conditions that would have favored greater deformation of the ejected material (Wright and Weinberg et al. 2009). These observations are also supported by the textural data: the high N_V^m values testify to rapid decompression of the magma, a phenomena associated with more rapid ascent rates from greater depths (Marsh 1988; 1998). In general, variations in the features of the emitted material reflect phases in which the conduit dynamics changed, although the eruptive intensity did not vary considerably. This is agrees with the data of Bonadonna et al. (2022) who report only small variations in plume height between LU, MU, and UU, mainly influenced by wind interaction, and relatively constant Mass Eruption Rate (MER) throughout the eruption.

5. Conclusions

The Tajogaite eruption of the Cumbre Vieja volcano (La Palma, Canary Islands) was a prolonged and complex hybrid eruption marked by changes in conduit dynamics that produced variable eruptive styles. A multidisciplinary study of the ejected juvenile material (variations in their physical, morphological, textural, and chemical features over time) has provided crucial information for understanding the processes that occurred during the pre-eruptive magma ascent and within the conduit system, which can be summarized as follows:

- Four main groups of juvenile fragments were identified that show wide variations in terms of morphology (solidity, convexity, axial ratio and CI values), vesicularity, vesicle population per unit volume melt (N_V^m), bubble size and shape, and glassy matrix composition. We suggest that these variations reflect different clast formation zones within the volcanic conduit system as well as different eruptive styles occurring both simultaneously and during different phases of the eruption.
- The three main stratigraphic units have been correlated with three main eruptive phases based on the characteristics of juvenile clasts:

  Phase I is initially marked by highly vesicular clasts (particularly Group 1), with irregular morphologies and spongy outer surfaces. The first stage of Phase I was characterized by a high eruptive intensity, dominated by the rapid ascent of volatile-rich magma and emplacement of discrete, massive beds of lapilli. Subsequently, the complete disappearance of Group 1 clasts and the appearance of Group 4 scoriaceous clasts are observed. Morphological and textural parameters cover wider ranges, and clast density increases. New magma pulses probably ascended at lower velocities along the conduits, favouring crystallization processes and resulting in the formation of more crystalline and dense material.

  Phase II is initially dominated by scoriaceous clasts of Group 4, marked by low vesicularity, high crystallinity and subspherical morphologies. The abundances of Groups 2 and 3 show lower values than the other phases. From the features of the material, we deduce that this stage was characterized by a change in eruptive dynamics probably caused by a slower ascent of partially degassed magma. Subsequently, the explosive activity continued with episodes of pulsatory intensity as also testified by more stratified tephra deposits characterized by alternation of ash and lapilli layers. The vesicularity of the clasts is variable and morphological parameters show the presence of both irregular and subspherical clasts with smooth to rough external surfaces. Groups 2 and 3 show higher abundances than the MU1 layer, while Group 4 clasts are minor. We suggest that at this stage, new pulses of more and variably outgassed magma have ascended at different velocities along the conduits, favouring coalescence and bubble collapse and resulting in the formation of clasts with wide ranges in textural and morphological features.

Phase III is marked by an initial lower abundance of Groups 2 and 3 clasts than in the later part of Phase II, and a higher amount of Group 4 clasts. Subsequently, abundances of Groups 2 and 3 clasts increase, while Group 4 clasts decrease. In particular, the strongly elongated clasts of Group 3 are present in increasing proportions. The vesicularity of the clasts is variable, and the densities are nearly constant with Phase II. From the features of the erupted material, we infer that the final phase was characterized by a new change in eruptive style. Batches of fluid magma ascended rapidly from narrow areas of the conduit, favouring overpressure conditions and high strain rates. This resulted in the formation of vesicular clasts, which exhibit collapse and coalescence phenomena of bubbles, as well as the formation of a significant amount of elongated and deformed clasts.

- Magma that fed the Tajogaite eruption falls overall in the tephritic-basanitic compositional range; however, as the eruption progressed, the glass chemistry became less evolved and shifted from tephritic to basanitic composition. The changes in these chemical concentrations as the eruption evolved could be associated with repeated inputs of more primitive and deeper magma, which perturbed the initial reservoir of more evolved magma and fuelled the eruption over time.

The multidisciplinary strategies applied for the characterization of fine-grained juvenile material by physical, morphological, textural, and chemical analyses have proven to be fundamental to the study of long-lasting, hybrid eruptions. These approaches advance the understanding of eruptive dynamics and provide essential tools for the mitigation of volcanic hazards, the protection of exposed populations and the management of volcanic crises in case of future, similar events.

References

Arzilli F, La Spina G, Burton MR, Polacci M, Le Gall N, Hartley ME, Di Genova D, Cai B,Vo NT, Bamber CE, Nonni S, Atwood R, Llewellin EW, Brooker A R, Mader HM, Lee PD (2019) Magma fragmentation in highly explosive basaltic eruptions induced by rapid crystallization. Nat. Geosci. 12:1023-1028.

Benito MB, Alvarado GE, Marchamalo M, Rejas JG, Murphy P, Franco R, Castro D, Garcia-Lanchares C, Sanchez J (2023) Temporal and spatial evolution of the 2021 eruption in the Tajogaite volcano (Cumbre Vieja rift zone, La Palma, Canary Islands) from geophysical and geodetic parameter analyses. Nat. Hazards 118(3): 2245-2284.

Bonadonna C, Pistolesi M, Biass S, Voloschina M, Romero J, Coppola D, Folch A, D'Auria L, Martin-Lorenz, A, Dominguez L, Pastore C, Reyes Hardy M, Rodríguez F (2022) Physical Characterization of Long-Lasting Hybrid Eruptions: The 2021 Tajogaite Eruption of Cumbre Vieja (La Palma, Canary Islands). J. Geophys. Res. https://doi.org/10.1029/2022jb025302

Bonadonna C, Pistolesi M, Dominguez L, Freret-lorgeril V, Rossi E, Fries A, Biass S, Voloschina M, Lemus J, Romero JE, Zanon V, Pastore C, Hardy MR, Sara L, Maio D, Gabellini P (2023) Tephra sedimentation and grainsize associated with pulsatory activity: the 2021 Tajogaite eruption of Cumbre Vieja (La Palma, Canary Islands, Spain). May, 1–24. https://doi.org/10.3389/feart.2023.1166073

Carracedo JC, Day S, Guillou H, Rodríguez Badiola E, Canas JA, Pérez Torrado FJ (1998) Hotspot volcanism close to a passive continental margin: The Canary Islands. Geol. Mag. 135(5): 591–604. https://doi.org/10.1017/S0016756898001447

Carracedo JC, Day SJ, Guillou H, Gravestock P (1999) Later stages of volcanic evolution of La Palma, Canary Islands: Rift evolution, giant landslides, and the genesis of the Caldera de Taburiente. AAPG Bulletin 111(5): 755–768. https://doi.org/10.1130/0016-7606(1999)111<0755:LSOVEO>2.3.CO;2

Carracedo JC, Badiola ER, Guillou H, De La Nuez J, Pérez Torrado FJ (2001) Geology and Volcanology of La Palma and El Hierro, Western Canaries. Estudios Geol, 57: 175–273.

Carracedo JC, Troll R, Day JMD, Geiger H, Aulinas M, Soler V, Deegan FM, Perez-Torrado FJ, Gisbert G, Gazel E (2022) The 2021 eruption of the Cumbre Vieja Volcanic Ridge on La Palma, Canary Islands. Geology Today, 38(3): 94–107.

Cashman KV, Stephen R, Sparks J, Blundy DJ (2017) Vertically extensive and unstable magmatic systems: a unified view of igneous processes. Science, 355 (6331) eaag3055. DOI: 10.1126/science.aag3055

Cioni R, Pistolesi M, Bertagnini A, Bonadonna C, Hoskuldsson A, Scateni B (2014). Insights into the dynamics and evolution of the 2010 Eyjafjallajökull summit eruption (Iceland) provided by volcanic ash textures. EPSL 394: 111–123. https://doi.org/10.1016/j.epsl.2014.02.051

Civico R, Ricci T, Scarlato P, Taddeucci J, Andronico D, Del Bello E, D'Auria L, Hernández PA, Pérez NM (2022) High-resolution Digital Surface Model of the 2021 eruption deposit of Cumbre Vieja volcano, La Palma, Spain. Scientific Data 9(1). https://doi.org/10.1038/s41597-022-01551-8

D'Auria L, Koulakov I, Prudencio J, Cabrera-Pérez I, Ibáñez JM, Barrancos J, García-Hernández R, Martínez van Dorth D, Padilla GD, Przeor M, Ortega V, Hernández P, Peréz NM (2022). Rapid magma ascent beneath La Palma revealed by seismic tomography. Scientific Reports 12(1). https://doi.org/10.1038/s41598-022-21818-9

Dayton K, Gazel E, Wieser P, Troll VR, Carracedo JC, La Madrid H, Roman DC, Ward J, Aulinas M, Geiger H, Deegan FM, Gisbert G, Perez-Torrado FJ (2023). Deep magma storage during the 2021 La Palma eruption. Science advances 9(6), eade7641. https://doi.org/10.1126/sciadv.ade7641

Dayton K, Gazel E, Wieser P, Troll V, Carracedo J, Aulinas M, Perez-Torrado F (2024) Magmatic storage and volatile fluxes of the 2021 La Palma eruption. Geochem. geophys. geosyst. 25(6) e2024GC011491. https://doi.org/10.1029/2024GC011491

Del Fresno C, Cesca S, Klügel A, Domínguez Cerdeña I, Díaz-Suárez EA, Dahm T, García-Cañada L, Meletlidis S, Milkereit C, Valenzuela-Malebrán C, López-Díaz R, López C (2023). Magmatic plumbing and dynamic evolution of the 2021 La Palma eruption. Nat. Commun 14(1): 358.

De Luca C, Valerio E, Giudicepietro F, Macedonio G, Casu F, Lanari R (2022) Pre- and Co-Eruptive Analysis of the September 2021 Eruption at Cumbre Vieja Volcano (La Palma, Canary Islands) Through DInSAR Measurements and Analytical Modeling. Geophys. Res. Lett. 49(7). https://doi.org/10.1029/2021GL097293

Di Nardo D, Padrón E, Rodríguez-Pérez C, Padilla GD, Barrancos J, Hernández PA, Asensio-Ramos M, Pérez NM (2022, May) Soil gas Rn monitoring at Cumbre Vieja prior and during the 2021 eruption, La Palma, Canary Islands. EGU22-10290. 10.5194/egusphere-egu22-10290

D'Oriano C, Del Carlo P, Andronico D, Cioni R, Gabellini P, Cristaldi A, Pompilio M (2022) Syn-eruptive processes during the January–February 2019 ash-rich emissions cycle at Mt. Etna (Italy): implications for petrological monitoring of volcanic ash. Front. Earth Sci.10, 824872. https://doi.org/10.3389/feart.2022.824872

Guillou H, Carracedo JC, Day SJ (1998) Dating of the upper Pleistocene–Holocene volcanic activity of La Palma using the unspiked K–Ar technique. J. Volcanol. Geotherm. Res. 86(1–4), 137–149. https://doi.org/10.1016/S0377-0273(98)00074-2

Guillou H, Carracedo JC, Duncan RA (2001) K–Ar, 40Ar–39Ar ages and magnetostratigraphy of Brunhes and Matuyama lava sequences from La Palma Island. J. Volcanol. Geotherm. Res. 106(3–4), 175–194. https://doi.org/10.1016/S0377-0273(00)00294-8

Houghton BF, Wilson CJN (1989) A vesicularity index for pyroclastic deposits. Bull. Volcanol 51, 451-462.

Houghton BF, Wilson CJN, Del Carlo P, Coltelli M, Sable JE, Carey R (2004) The influence of conduit processes on changes in style of basaltic Plinian eruptions: Tarawera 1886 and Etna 122 BC. J. Volcanol. Geotherm. Res. 137(1-3), 1-14. https://doi.org/10.1016/j.jvolgeores.2004.05.009

Klügel A, Galipp K, Hoernle K, Hauff F, Groom S (2017) Geochemical and volcanological evolution of la palma, Canary Islands. J Petrol 58(6): 1227–1248. https://doi.org/10.1093/petrology/egx052

Klügel A, Hoernle KA, Schmincke HU, White JDL (2000) The chemically zoned 1949 eruption on La Palma (Canary Islands): Petrologic evolution and magma supply dynamics of a rift zone eruption. J. Geophys. Res. 105(B3): 5997–6016. https://doi.org/10.1029/1999jb900334

Kueppers U, Scheu B, Spieler O, Dingwell DB (2006) Fragmentation efficiency of explosive volcanic eruptions: a study of experimentally generated pyroclasts. J. Volcanol. Geotherm. Res. 153(1-2): 125-135. https://doi.org/10.1016/j.jvolgeores.2005.08.006

Liu EJ, Cashman KV, Rust AC (2015) Optimising shape analysis to quantify volcanic ash morphology. GeoResJ, 8, 14-30. https://doi.org/10.1016/j.grj.2015.09.001

Marsh BD (1988) Crystal size distribution (CSD) in rocks and the kinetics and dynamics of crystallization: I. Theory. Contrib. Mineral. Petrol. 99: 277-291.

Marsh BD (1998) On the interpretation of crystal size distributions in magmatic systems. J Petrol 39(4): 553-599. https://doi.org/10.1093/petroj/39.4.553

Pankhurst MJ, Scarrow JH, Barbee OA, Hickey J, Coldwell BC, Rollinson GK, Rodríguez-Losada JA, Lorenzo AM, Rodríguez F, Hernández W (2022) Rapid response petrology for the opening eruptive phase of the 2021 Cumbre Vieja eruption, La Palma, Canary Islands. Volcanica, 5(1), 1–10.

Pioli L, Erlund E, Johnson E, Cashman K, Wallace P, Rosi M, Granados HD (2008) Explosive dynamics of violent Strombolian eruptions: the eruption of Parícutin Volcano 1943–1952 (Mexico). EPSL 271(1-4): 359-368. https://doi.org/10.1016/j.epsl.2008.04.026

Pioli L, Azzopardi BJ, Cashman KV (2009) Controls on the explosivity of scoria cone eruptions: Magma segregation at conduit junctions. Journal of Volcanology and Geothermal Research, 186(3-4): 407-415. https://doi.org/10.1016/j.jvolgeores.2009.07.014

Pioli L, Azzopardi BJ, Bonadonna C, Brunet M, Kurokawa AK (2017) Outgassing and eruption of basaltic magmas: The effect of conduit geometry. Geology,45(8): 759-762 https://doi.org/10.1130/G38787.1

Pistolesi M, Cioni R, Bonadonna C, Elissondo M, Baumann V, Bertagnini A, Chiari L, Gonzales R, Rosi M, Francalanci L (2015) Complex dynamics of small-moderate volcanic events: the example of the 2011 rhyolitic Cordón Caulle eruption, Chile. Bull. Volcanol. 77: 1-24. https://dx.doi.org/10.1007/s00445-014-0898-3

Reyes-Hardy MP, Biass S, Dominguez L, Di Maio LS, Frischknecht C, Bonadonna C, Pérez N (2024) Temporal evolution of roof collapse from tephra fallout during the 2021-Tajogaite eruption (La Palma, Spain). Front. Earth Sci. 11, 1303330. https://doi.org/10.3389/feart.2023.1303330

Rodríguez-Pérez C, Barrancos J, Hernández PA, Pérez NM, Padrón E, Melián GV, Rodríguez F, Asensio-Ramos M, Padilla GD (2022, May) Continuous monitoring of diffuse CO2 emission from Cumbre Vieja volcano: early evidences of magmatic CO2 surface arrival. EGU22-9819 10.5194/egusphere-egu22-9819

Rodríguez F, Coldwell B, Martín-Lorenzo A, Andronico A, Bonadonna C, Del Bello E, Pistolesi M, Taddeucci J, Biass s, Romero JE, Voloschina M, Scarlato P, Hernández W, D'Auria L, M. Pérez N, (2024) Towards rapid integrated data acquisition and management during a volcanic crisis: the 2021 Tajogaite eruption of Cumbre Vieja (La Palma, Canary Islands). Volcanica

Romero JE, Burton M, Cáceres F, Civico R, Ricci T, Pankhurst MJ, Hernández PA, Bonadonna C, Llewellin EW, Pistolesi M, Polacci M, Solana C, Auria D, Arzilli F, Andronico D, Rodríguez F, Asensio-ramos M, Martín-lorenzo A, Hayer C (2022) The initial phase of the 2021 Cumbre Vieja ridge eruption (Canary Islands): Products and dynamics controlling edifice growth and collapse. J. Volcanol. Geotherm. Res. 107642. https://doi.org/10.1016/j.jvolgeores.2022.107642

Sahagian D L, Proussevitch A A (1998) 3D particle size distributions from 2D observations: Stereology for natural applications. J. Volcanol. Geotherm. Res. 84(3–4): 173–196. https://doi.org/10.1016/S0377-0273(98)00043-2

Schneider CA, Rasband WS, Eliceiri KW (2012) NIH Image to ImageJ: 25 years of image analysis. Nature methods, 9(7): 671-675.

Shea T, Houghton BF, Gurioli L, Cashman KV, Hammer JE, Hobden BJ (2010) Textural studies of vesicles in volcanic rocks: An integrated methodology. J. Volcanol. Geotherm. Res. 190(3–4): 271–289. https://doi.org/10.1016/j.jvolgeores.2009.12.003

Sparks RSJ (2003) Dynamics of magma degassing. https://doi.org/10.1144/GSL.SP.2003.213.01.02

Staudigel H, Feraud G, Giannerini G (1986) The history of intrusive activity on the island of La Palma (Canary Islands). J. Volcanol. Geotherm. Res. *27*(3-4): 299-322. https://doi.org/10.1016/0377-0273(86)90018-1

Taddeucci J, Pompilio M, Scarlato P (2002) Monitoring the explosive activity of the July–August 2001 eruption of Mt. Etna (Italy) by ash characterization. Geophys. Res. Lett. 29(8). https://doi.org/https://doi.org/10.1029/2001GL014372

Taddeucci J, Pompilio M, Scarlato P (2004). Conduit processes during the July–August 2001 explosive activity of Mt. Etna (Italy): inferences from glass chemistry and crystal size distribution of ash particles. J. Volcanol. Geotherm. Res. 137(1): 33–54. https://doi.org/https://doi.org/10.1016/j.jvolgeores.2004.05.011

Taddeucci J, Scarlato P, Andronico D, Ricci T, Civico R, Del Bello E, Spina L, D'Auria L, Asensio-Ramos M, Calvo D, Padrón E, Hernández PA, Pérez NM (2023) The explosive activity of the 2021 tajogaite eruption (La Palma, canary islands, Spain). Geochem. geophys. geosyst. 24(6), e2023GC010946. https://doi.org/10.1029/2023GC010946

Ubide T, Márquez Á, Ancochea E, Huertas M J, Herrera R, Coello-Bravo JJ, Sanz-Mangas D, Mulder J, Macdonald A, Galindo I (2023) Discrete magma injections drive the 2021 La Palma eruption. 4813. https://doi.org/10.1126/sciadv.adg4813

Wertheim D, Coldwell B, Miyashita L, Gill I, Crust S, Giddens R, Pérez NM, Petford N, Grigg J (2023) Confocal microscopy 3D imaging and bioreactivity of La Palma volcanic ash particles. Sci. Total Environ. 899: 165647. https://doi.org/10.1016/j

Wright HM, Weinberg RF (2009) Strain localization in vesicular magma: Implications for rheology and fragmentation. Geology, 37(11): 1023-1026. https://doi.org/10.1130/G30199A.1

Zanon V, D'Auria L, Schiavi F, Cyrzan K, Pankhurst MJ (2024) Toward a near real-time magma ascent monitoring by combined fluid inclusion barometry and ongoing seismicity. Science Advances, 10(6), eadi4300. https://doi.org/10.1126/sciadv.adi4300

Acknowledgments

The authors are grateful to the Instituto Volcanológico de Canarias (INVOLCAN) for the logistic support that was key to the development of this work. The Center for Instrument Sharing of the University of Pisa (CISUP) is acknowledged for assistance during tephra imaging with FEG-SEM used for textural analyses and Center for Electron Microscopy and Microanalysis Services of the University of Florence (MEMA) for assistance during electron microprobe analysis (EMPA).

Funding

Research activities were supported by the Swiss National Science Foundation (Grant #200020_188757).

Data availability

All data in the manuscript is presented in the figures and in the tables of the Supplementary Material.

Competing interests

The authors declare no competing interests.

Author Contribution

CB and MP have organized the field campaigns, acquired the funding, and planned the work. CB, MP, MV, BCC have participated in the field work and contributed to data collection. SDM, CB, MP, MV have contributed to data processing. SDM, MP, MV, CB, and BCC have produced the original draft of the paper and designed the tables and figures. All authors have participated in overall discussions and editing of the manuscript.

Fig 1

Click here to access/download;Figure;Fig 1.tif

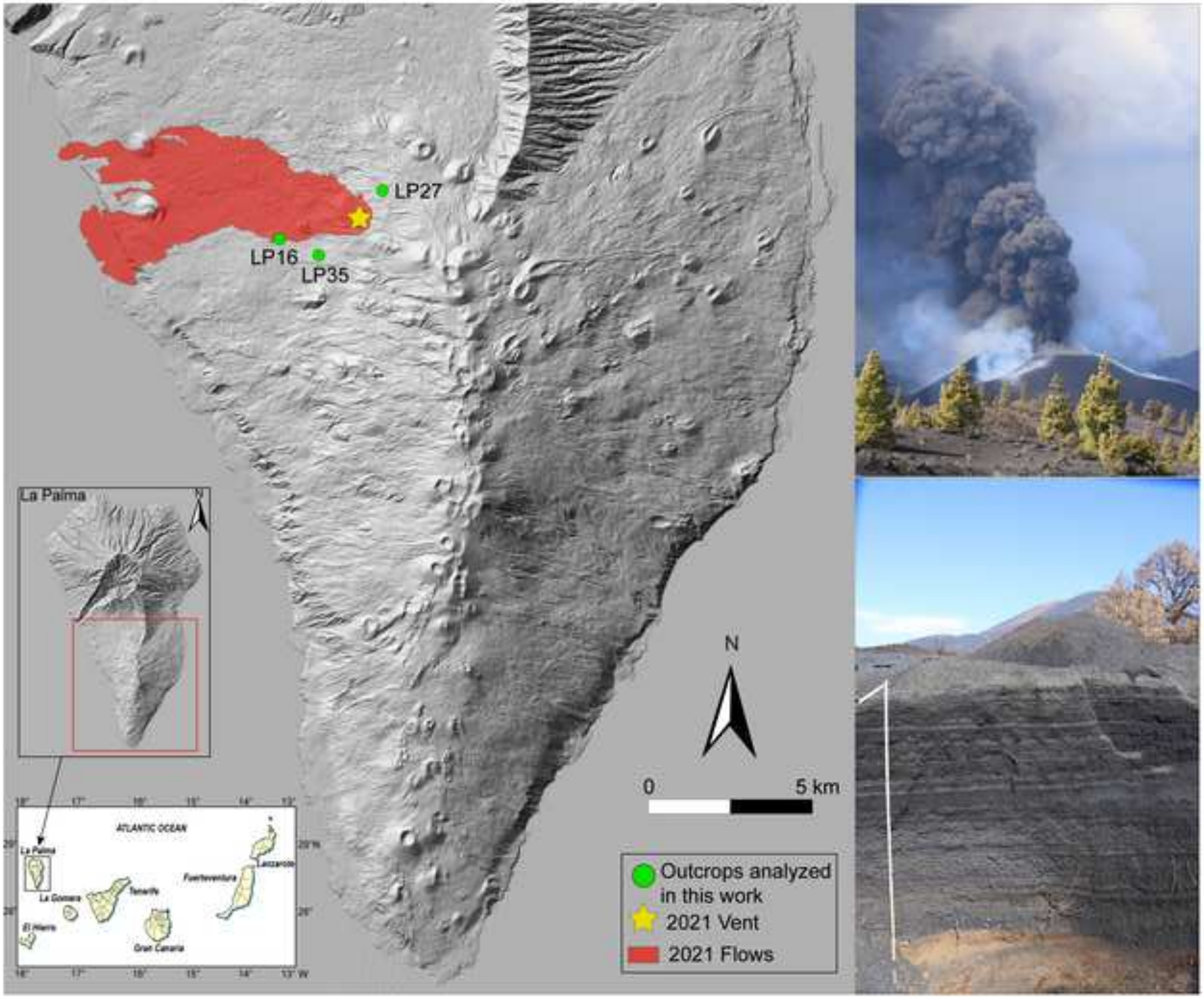

Fig 2 Click here to access/download;Figure;Fig 2.tif

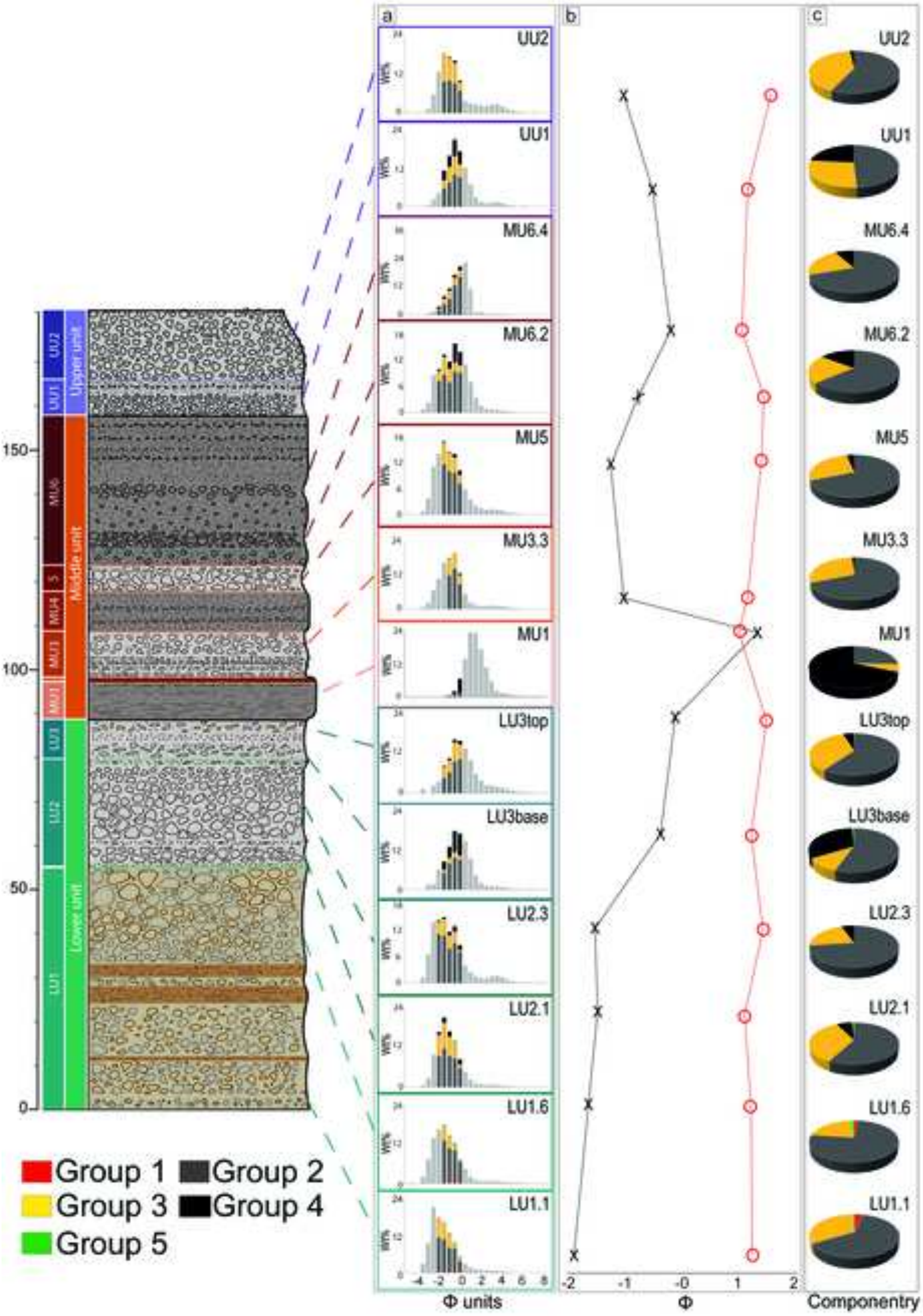

Fig 3

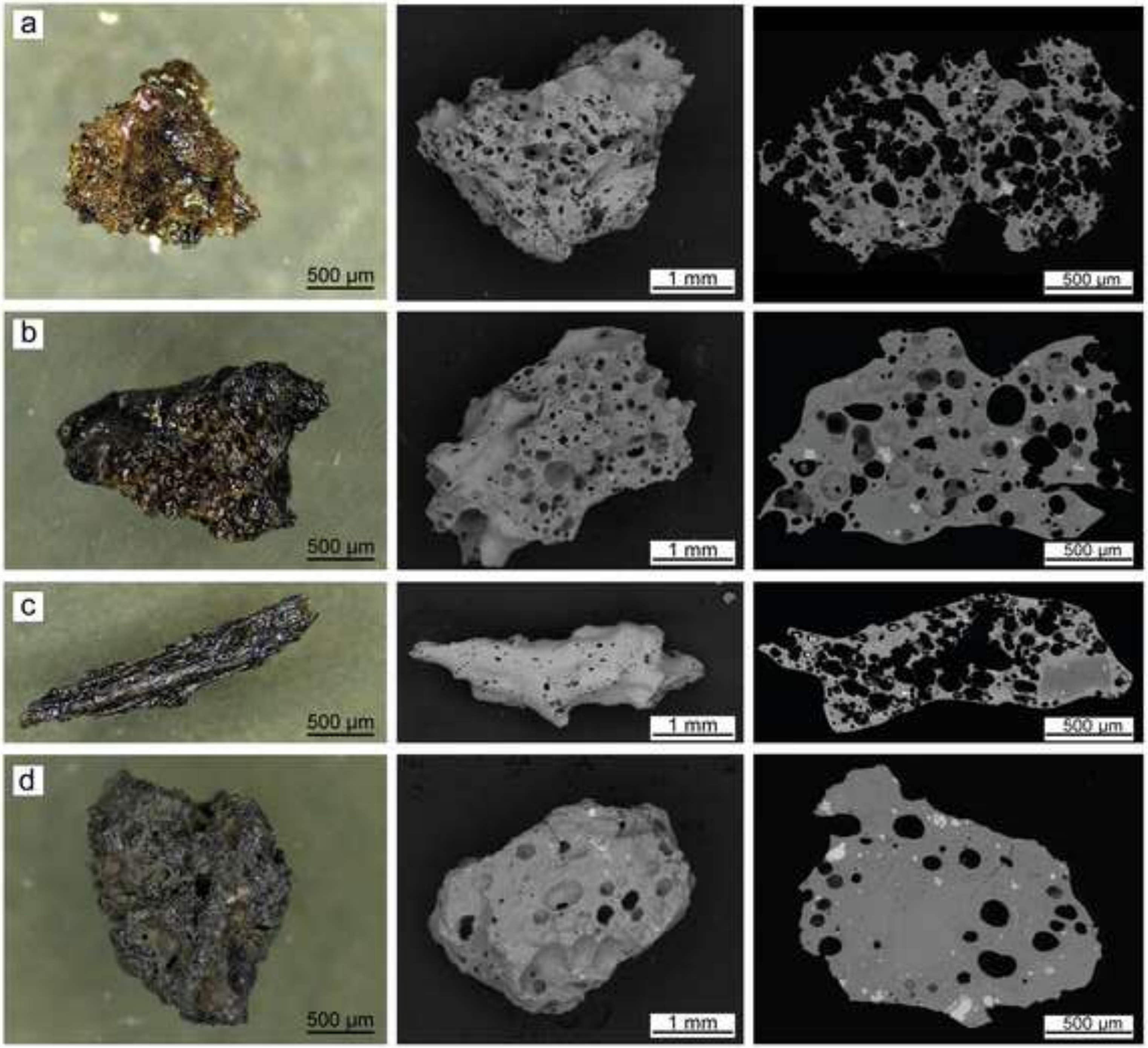
a
500 µm
1 mm
500 µm
b
500 µm
1 mm
500 µm
c
500 µm
1 mm
500 µm
d
500 µm
1 mm
500 µm

Fig 4

Click here to access/download;Figure;Fig 4.tif

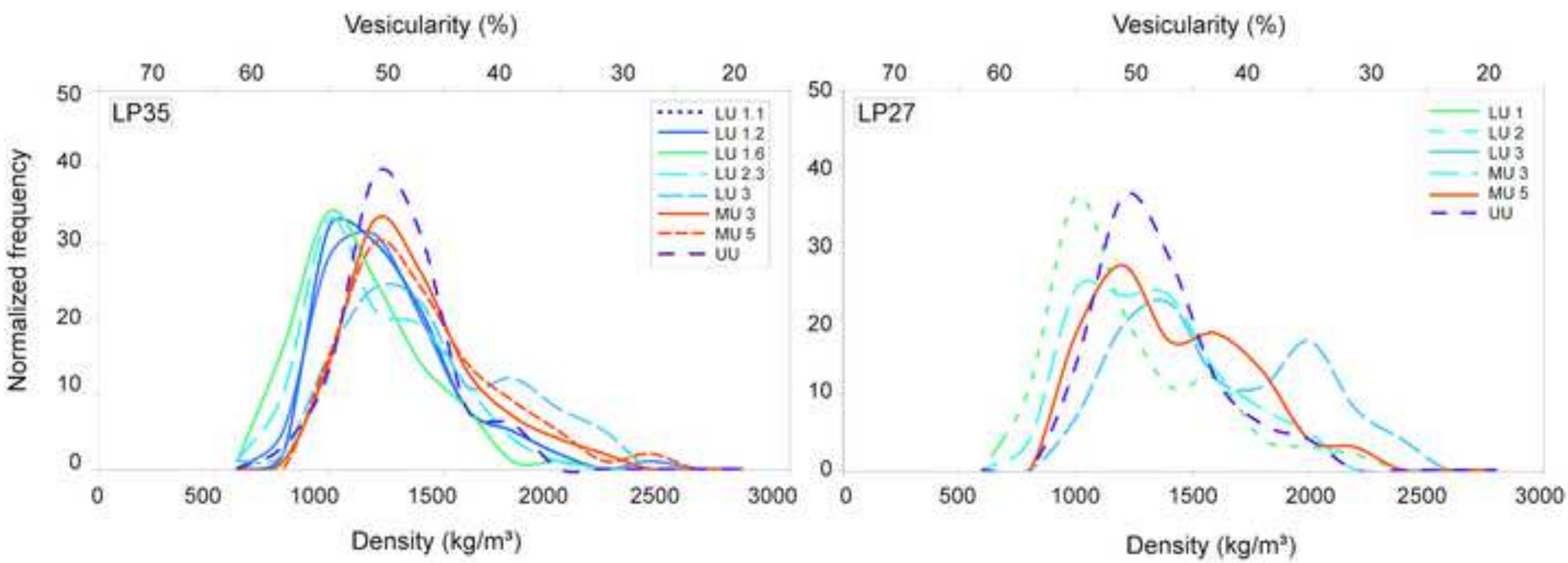

Fig 5

Click here to access/download;Figure;Fig 5.tif

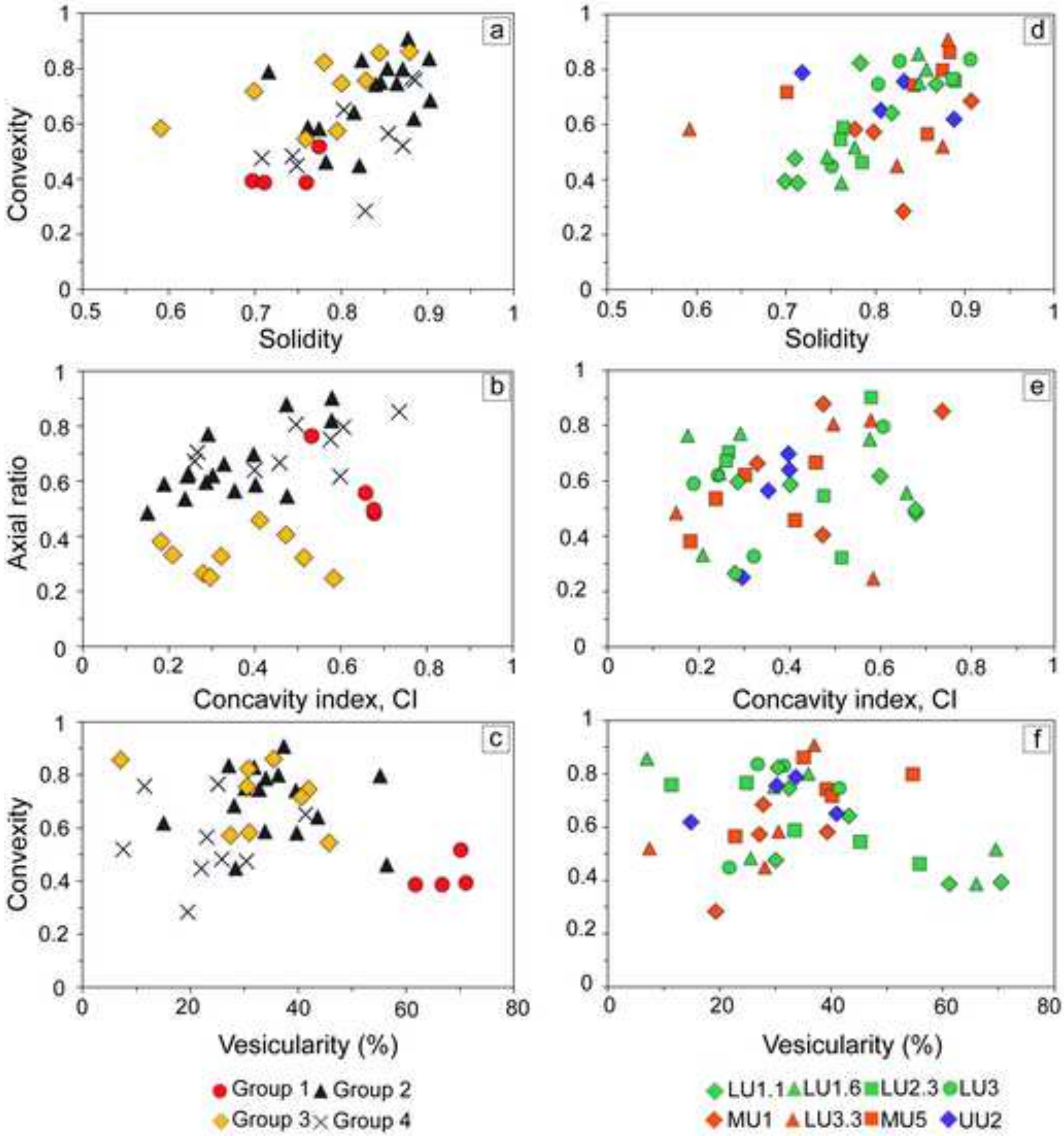

Fig 6

Click here to access/download;Figure;Fig 6.tif

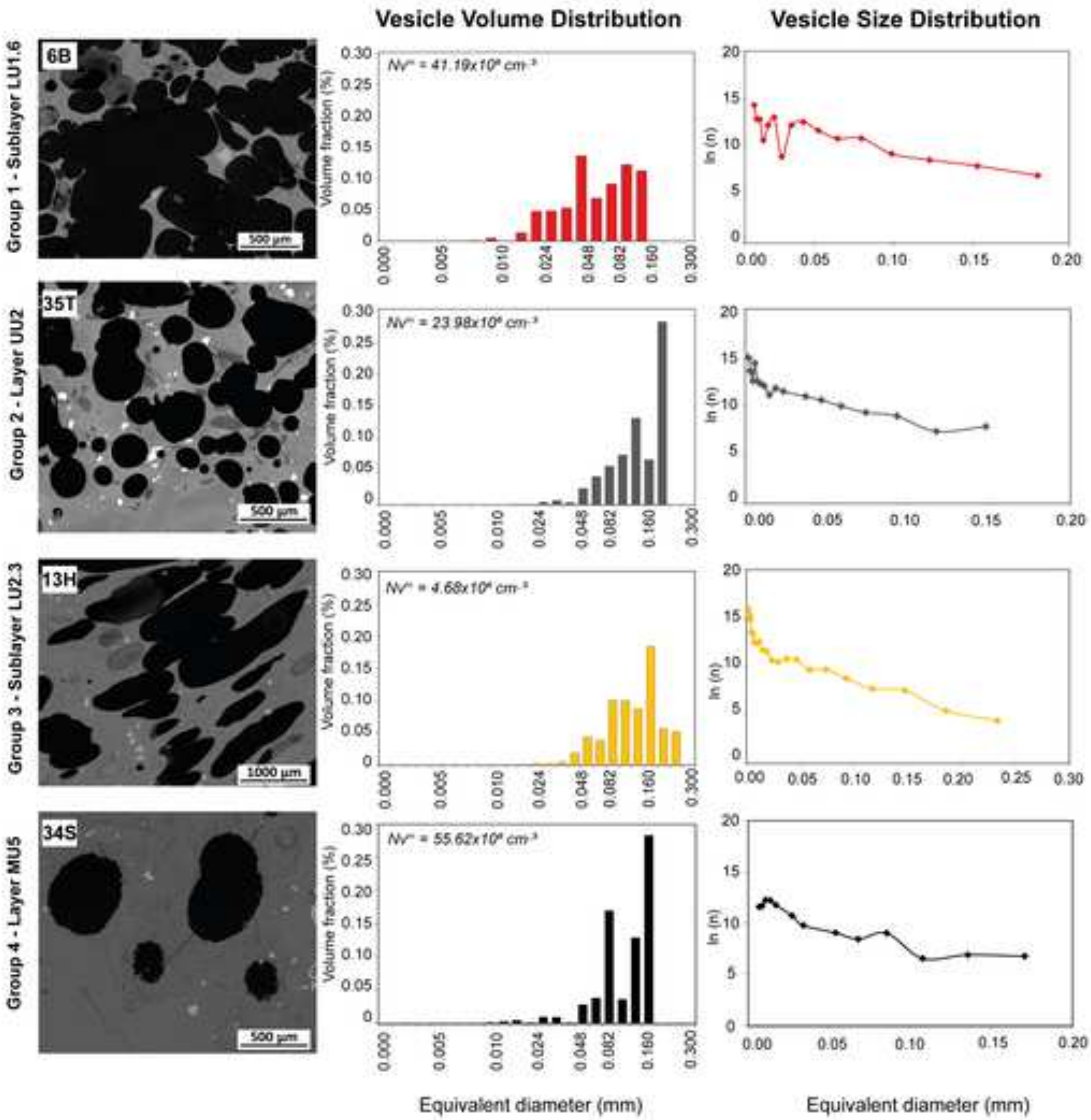

Fig 7

Click here to access/download;Figure;Fig 7.tif

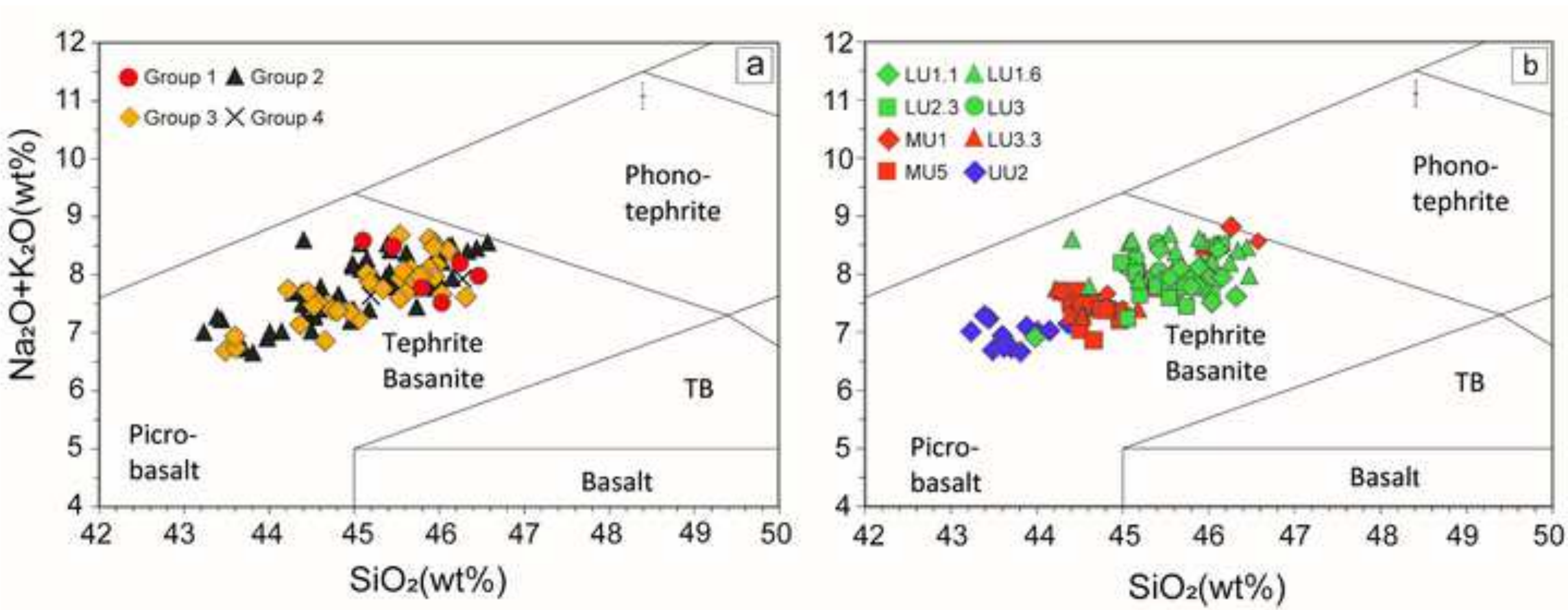

Fig 8

Click here to access/download;Figure;Fig 8.tif

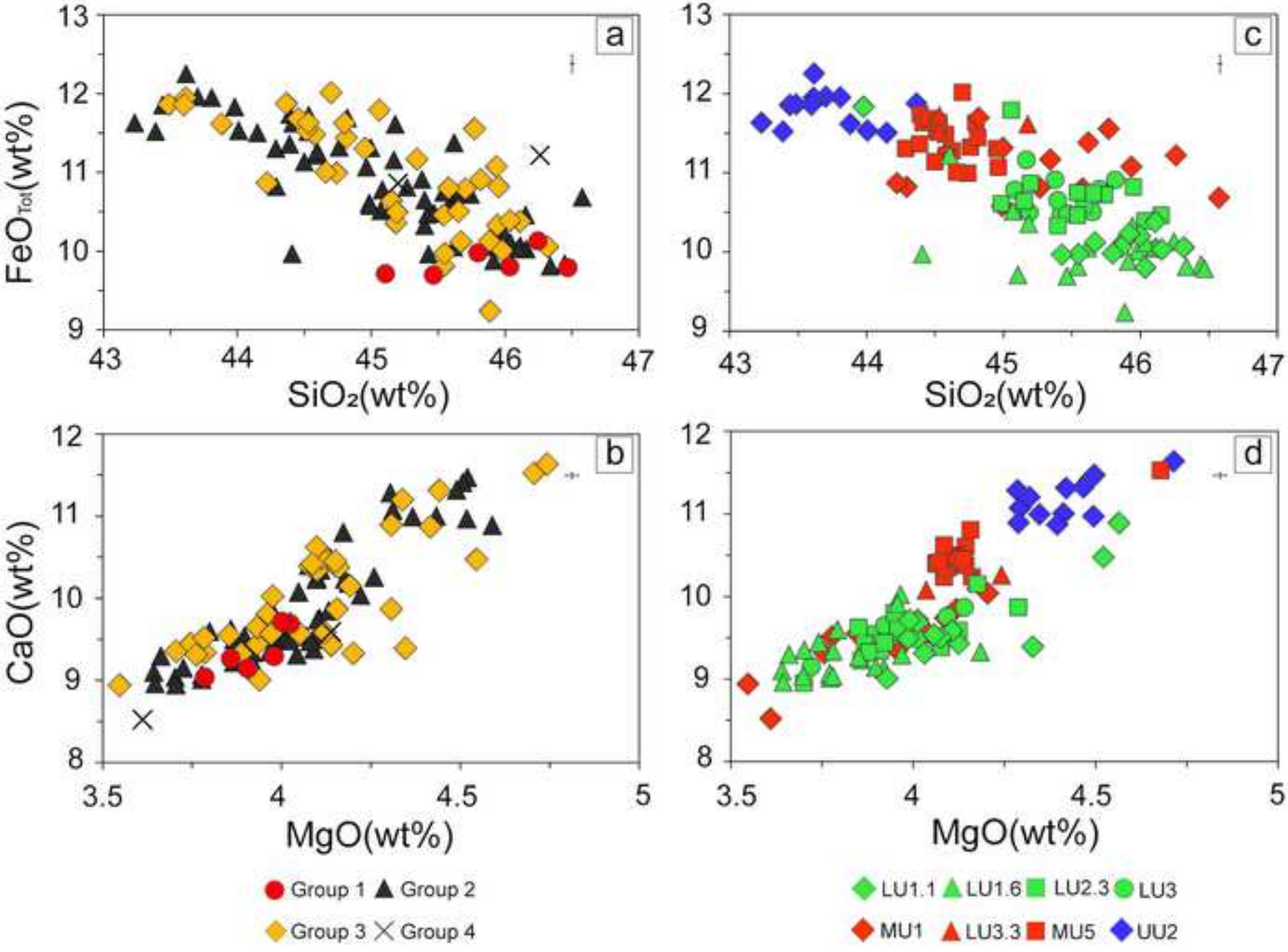

Fig 9

Click here to access/download;Figure;Fig 9.tiff

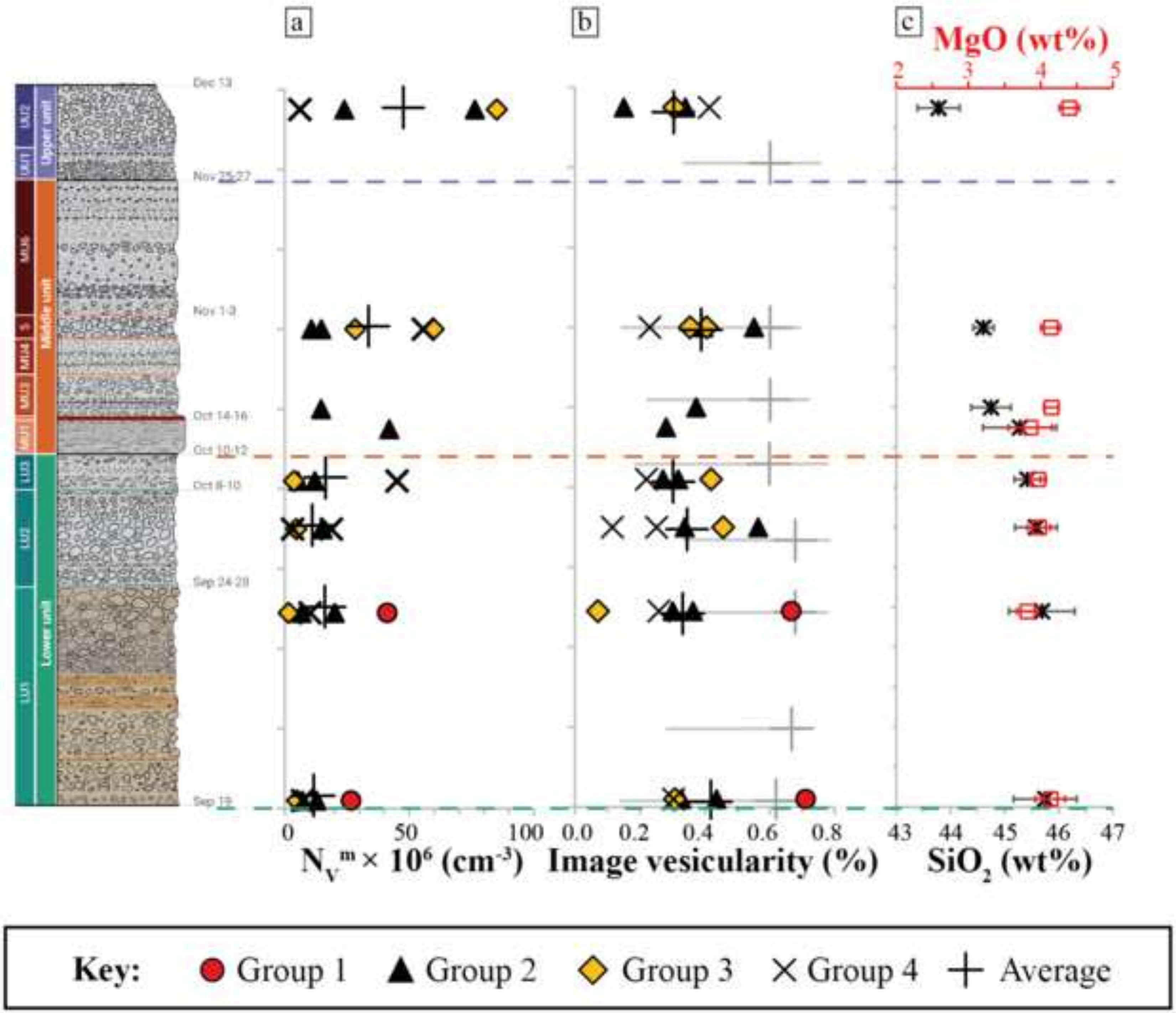

Fig S1

Click here to access/download
Supplementary Material
Fig S1.tif

Fig S2

Click here to access/download
Supplementary Material
Fig S2.tif

Fig S3

Table S1

Click here to access/download
Supplementary Material
Table S1.xlsx

Table S2

Click here to access/download
Supplementary Material
Table S2.xlsx

Table S3

Click here to access/download
Supplementary Material
Table S3.xlsx